Constraining Rain Evaporation during the EUREC^{4}A Campaign with the Super-Droplet-Model CLEO

Master Thesis

M. Sc. Climate Physics

Christian-Albrechts-Universität Kiel
GEOMAR Helmholtz Center for Ocean Research
Max Planck Institute for Meteorology

Author: Nils Niebaum

Matriculation Number: 1118884

First Examiner: Prof. Dr. Joakim Kjellsson

Second Examiner: Prof. Dr. Raphaela Vogel

Special thanks to: Clara Bayley
Dr. Ann Kristin Naumann

September 19, 2024

Abstract

The evaporation of rain below the cloud base is a crucial process and affects surface precipitation as well as the energy balance of the sub cloud layer of shallow convective trade cumulus clouds and their mesoscale organization. We estimate rain evaporation and its associated latent cooling, using the newly developed Super-Droplet-Model CLEO in an 1D rainshaft implementation, based on thermodynamic profiles and Droplet Size Distributions (DSD) from 111 individual clouds, measured during the EUREC^{4}A campaign.

Our estimated inter-cloud mean latent cooling of $32.7\,\mathrm{W\,m^{-2}}$ and our rain evaporated fraction of $7.1\,\%$ are lower than in previous studies, most likely due to our underestimation of cloud base liquid water content (LWC) and differing DSDs. We find the cloud base LWC to be the primary constrain of cloud specific column integrated latent cooling, explaining approximately $50\,\%$ of its variability. We identify the gradient of relative humidity to determine the shape of the cloud's latent cooling profiles.

With our novel approach we are able to incorporate collisional coalescence, breakup and rebound of droplets. Coalescence systematically reduces laten cooling by up to $10\,\%$ near the surface, while breakup enhances it due to fragmentation of large rain droplets into smaller ones. However, these effects are small compared to the inter-cloud spread. We hereby give confidence, that also methods excluding droplet-droplet interactions can yield good estimates of rain evaporation.

Further sensitivity experiments and comparisons with other models and radar-retrieval methods will be necessary to give more robust estimations of rain evaporation and associated uncertainties.

Table of Contents

1 Introduction

Below every precipitating cloud, rain droplets pass through unsaturated air on their way towards the surface and thus partly evaporate, reducting surface precipitation and moistening and cooling the surrounding air masses. By triggering down drafts, the denser, colder and moister air spreads horizontally along the surface, forming cold pools, which in turn trigger a chain of dynamic processes and influence the mesoscale cloud organization and cloud cover (Li et al., 2014; Nuijens et al., 2014; Touzé-Peiffer et al., 2022).

In the trade wind regions, shallow cumulus clouds are the most common cloud type and often referred to as trade cumulus clouds. Especially deeper trade cumulus clouds of $2\,\mathrm{km}$ to $3\,\mathrm{km}$ thickness cause precipitation during their lifecycle (Nuijens et al., 2009; Stevens, 2005; Vogel et al., 2021). Because the trade regions are relatively dry, rain evaporation is enhanced and leads to a favourable environment for cold pool formation. Cold pools can be found approximately $8\,\%$ of the time, while they are more prominent in the boreal summer months (Touzé-Peiffer et al., 2022; Vogel et al., 2021). Due to their impact on cloud organization, they can modulate the cloud radiative effect and thus can impact trade wind cumulus cloud feedbacks (Vogel et al., 2021). Because cloud feedbacks of shallow clouds over the ocean are still a major source of uncertainty in our estimation of earths climate sensitivity, a deeper understanding of these processes is necessary (Bony & Dufresne, 2005; Bony et al., 2015, 2020; Vial et al., 2017). Understanding these mechanisms better, help to model clouds and precipitation more accurate in weather- and climate-models.

Direct measurement of rain evaporation is not trivial, because it would require measurements of the droplet size distribution (DSD) and its vertical evolution at and below the cloud base. Aircraft in-situ probes give the most direct and accurate estimate of droplet size distribution (DSD) from within clouds and at the cloud bases. Using measured cloud base DSD, Sarkar et al., 2023 simulated the rain evaporation with a 1D rainshaft model based on a microphysical bin scheme. They used the DSD measured on the NOAA P3 aircraft during the ATOMIC campaign at different flight heights (Leandro & Chuang, 2021; Pincus et al., 2021) and simulated the vertical evolution of the DSD for individual days, with an idealized relative

humidity profile. They found $63\,\%$ of the rain mass to evaporate in the sub cloud layer, and a spread in latent cooling of $15\,\mathrm{W\,m^{-2}}$ to $352\,\mathrm{W\,m^{-2}}$ or equivalently $2\,\mathrm{K\,d^{-1}}$ to $50\,\mathrm{K\,d^{-1}}$. The evaporation profiles showed a stronger evaporation near the cloud base than above the surface (top-heavy) for most profiles, and more evaporation near the surface (bottom-heavy) for a minority of profiles. Sarkar et al., 2023 identified the shape and mean radius of the DSD to control the top- vs. bottom-heaviness, having more large rain droplets favoring bottom-heaviness The measured cloud liquid water content (LWC) was a dominant constrain on the column integrated vertical evaporation rate.

Robustly measuring DSD in the sub cloud layer is still ongoing research. Tridon et al., 2017 developed a method to retrieve the DSD from Doppler velocity spectra measured with K_a and W band Doppler radars. They were able to estimate the DSD of rain droplets over a large range of altitudes for rain droplets with radii above $0.15\,\mathrm{mm}$. Tridon et al., 2017 retrieved evaporative latent cooling rates to range from $19.2\,\mathrm{K\,d^{-1}}$ to $30\,\mathrm{K\,d^{-1}}$ in the sub cloud layer between $1\,\mathrm{km}$ altitude and the $3\,\mathrm{km}$ high cloud base from a deeper continental convection over the Great Plains (US) with heavy rain rates exceeding $0.5\,\mathrm{mm\,h^{-1}}$ for a measurement period of $1.5\,\mathrm{h}$. The strongest evaporation rates were found in the middle to lower altitudes of the sub cloud layer [1]. The large spread of evaporation rates between individual simulations by Sarkar et al., 2023 and the larger uncertainties in the method of Tridon et al., 2017 highlight the challenge in constraining the magnitude, variability and vertical structure of rain evaporation. Due to the lack of long term observations, it is difficult to robustly estimate rain evaporation and disentangle the various factors influencing rain evaporation.

Apart from the ambient humidity profiles and the clouds properties (e.g. cloud base height, DSD), droplet microphysics can strongly impact precipitation and rain evaporation rates. Bao and Windmiller, 2021 showed that different terminal velocity magnitudes, by altering the evaporation efficiency, can impact extreme precipitation and cloud organization in storm-resolving simulations. Further, the collision of droplets, resulting either in coalesce into a new larger droplet, rebound or breaking up into smaller fragments, can strongly alter the DSD below cloud base (Hu & Srivastava, 1995; Seifert, 2008).

In order to understand the impact of the DSD and droplet-droplet interaction on rain evaporation, it is crucial to take a step back and understand how different droplet radii, r, in-

[1] Using the specific heat capacity of air of $1.21 \times 10^3\,\mathrm{J\,m^{-3}\,K^{-1}}$ this would be $0.27\,\mathrm{W\,m^{-3}}$. Assuming constant vertical cooling for a $700\,\mathrm{m}$ thick sub cloud layer, as in Sarkar et al., 2023, the values convert to $188\,\mathrm{W\,m^{-2}}$ and $293.75\,\mathrm{W\,m^{-2}}$ respectively.

fluence evaporation. The evaporation rate of a droplet is proportional to its surface area ($\propto r^2$), whereas its mass is proportional to its volume ($\propto r^3$) (Köhler, 1936; Lohmann et al., 2016; Rogers & Yau, 1989). Large droplets have a larger surface area, allowing them to evaporate more mass than small droplets in a given time. However, small droplets evaporate a larger fraction of their mass in a given time, because they have a larger ratio of surface against mass. Therefore, smaller droplets have a higher evaporation efficiency.

Other studies already provided a useful methodology for studying rain evaporation (Sarkar et al., 2023; Tridon et al., 2017; Wood, 2005), but they do not account for droplet-droplet interactions, which can strongly alter the sub cloud layer DSD (Hu & Srivastava, 1995; Seifert, 2008). More generally, the simulation of rain processes with bulk and bin microphysical schemes still carry a lot of uncertainties, and large inter-scheme differences exist (vanZanten et al., 2011). Motivated by these needs, we use the novel Super-Droplet-Model CLEO, which is capable to model microphysical processes in warm clouds (Bayley, 2024a; Bayley et al., n.d.). The Super-Droplet-Model was introduced by Shima et al., 2009 as a new Lagrangian approach to model cloud microphysics, by representing a group of similar droplets with comparable radius, velocity, and mass of solute with individual super-droplet. The multiplicity of a super-droplet accounts for the number of real droplets it represents, and the interaction between droplets is modelled probabilistically (Bayley et al., n.d.; Shima et al., 2009). While classical bin and bulk schemes model the evolution of the DSD directly, a Super-Droplet-Model simulates the evolution of the individual super-droplets. The super-droplets behave almost like real droplets, allowing the Super-Droplet-Model to be closer related to our physical understanding of microphysical processes in clouds (Grabowski et al., 2018; Morrison et al., 2020).

We use CLEO in a 1D rainshaft setup to estimate the state of the sub cloud layer, similar to Sarkar et al., 2023 and Seifert, 2008. We model a snapshot of the sub cloud layer from the evolution of individual trade cumulus clouds. We use observations of DSD near cloud base and thermodynamic profiles from the EUREC^{4}A campaign within our model. Other than Sarkar et al., 2023, we simulate the rain evaporation for individual clouds with unique DSD and thermodynamic profiles of the sub cloud layer. We define four setups with hierarchical inclusions of microphysics droplet collision processes.

In this study, we first describe the observational datasets used (Section 2.1), then explain how we processed the observations to be incorporated into our model (Section 2.2), followed by a description of the model setup (Section 2.3). In Chapter 3 we investigate the following questions:

- Does our setup produce realistic results?
- What is the influence of cloud properties and thermodynamics on rain evaporation?
- How does the DSD influence the evaporation rate?
- How sensitive is rain evaporation to the different microphysical processes?

We summarize and discuss our findings in Chapter 4 and provide an outlook on future projects and remaining questions.

2 Data and Methods

2.1 Observational data

We use two observational datasets from the EUREC^{4}A campaign (ElUcidating the RolE of Clouds-Circulation Coupling in ClimAte), to retrieve the necessary DSD at cloud base, the cloud base height and the thermodynamic profiles below the cloud base. All observational data which we use in this study can be seen in Figure 1. The broader goal of the EUREC^{4}A campaign was to understand and quantify the interaction of cloud properties and the atmospheric and oceanographic environment across a large range of scales, from the microphysics to the mesoscale, in the trade wind regions (Stevens et al., 2021). It took place in the tropical North Atlantic east and southeast of Barbados in 2020 from January 20th to February 20th.

Cloud base Droplet Size Distribution (DSD)

We get the cloud base DSD from the SAFIRE ATR42: PMA/Cloud composite dataset (cloud composite) dataset (Coutris, 2021). It contains the DSD for cloud, drizzle and rain droplets along the ATR aircraft flight track at a $1\,\mathrm{Hz}$ resolution. Because the ATR flew with roughly $100\,\mathrm{m\,s^{-1}}$, the distance between individual measurements of $1\,\mathrm{s}$ is equivalent to approximately $100\,\mathrm{m}$. The measured DSD is a composition of the data from the CDP-2 instrument for cloud droplets and the 2D-S instrument for drizzle and rain droplets. It covers a droplet radii range from $1\,\mu\mathrm{m}$ to $1.275\,\mathrm{mm}$ radii given in non-uniform bin widths (Bony et al., 2022; Coutris, 2021). We use data from 19 cloud base rectangular flight tracks flown east of Barbados over 11 days.

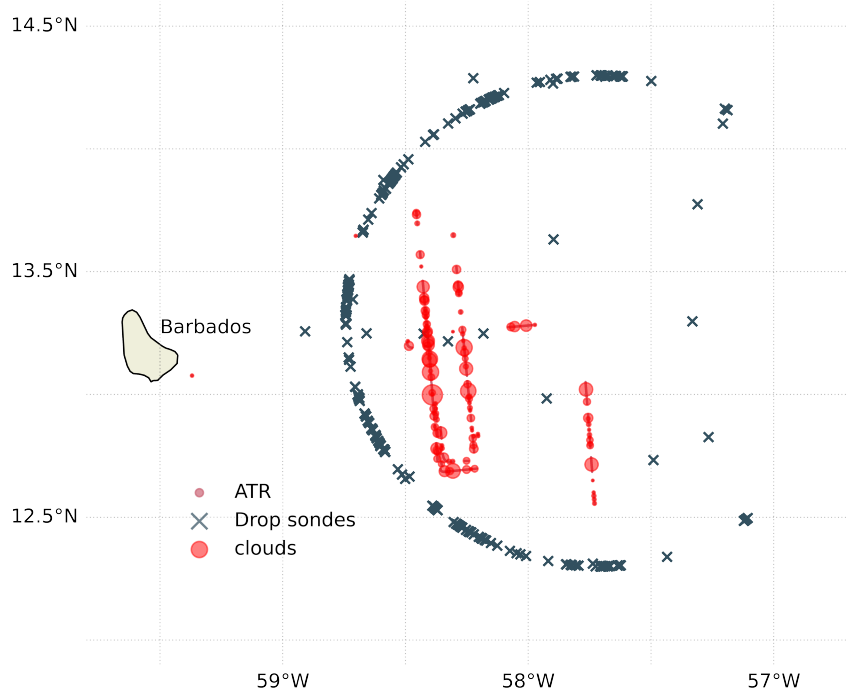

Figure 1: All observations used in this study from the tropical North Atlantic near Barbados (pastel). Identified clouds shown as transparent big red circles with the size proportional to their horizontal extent. Cloud base DSD measured by the ATR aircraft (cloud-composite dataset) as small light-red dots. Drop sonde release positions from the JOANNE dataset as dark-blue crosses.

Thermodynamic profiles

We get humidity and temperature profiles from the Level 3 Version 2.0.0 of the JOANNE dataset (Joint dropsonde Observations of the Atmosphere in tropical North atlaNtic mesoscale Environments) (George, 2021; George et al., 2021). The individual thermodynamic profiles were measured by drop sondes released from the HALO and P3 aircraft along circles of $220\,\mathrm{km}$ diameter. All profiles have a vertical resolution of $10\,\mathrm{m}$.

2.2 Methods

2.2.1 Rain cloud selection

We identify individual rain clouds in the cloud composite dataset and treat them separately. In a first step, we identify all measurements containing rain droplets, by using the rain mask provided within the dataset. The rain mask marks a measurement as rainy, if rain droplets

with a radius of at least $R \geq 250\,\mu\mathrm{m}$ were measured (Bony et al., 2022). Because the concentration of rain droplets is very low compared to the measurement volume of the devices ($30\,\mathrm{cm}^3$), we relax this criterion slightly, by allowing 5 consecutive rain free measurements in-between each rain measurement. From this new identification mask, consecutive values form an individual clouds. A small illustration of this can be seen in Figure S1. With this setup, we can identify 405 rain clouds in the whole dataset.

We further select clouds based on the following criteria, leaving us with a set of 125 individual clouds:

- Because we are only interested in the DSD near cloud base, we restrict the cloud to be within $500\,\mathrm{m}$ to $1200\,\mathrm{m}$ altitude. Bony et al., 2022 found this to be a reasonable height of the cloud base for all days of the campaign (see their Table 1).
- We only use clouds from horizontally flown ATR flight track.
- Clouds need to consist of at least three consecutive measurements, thus have a horizontal extent of at least roughly $300\,\mathrm{m}$.

Not only are cloud properties like DSD strongly linked to the cloud type, but also the thermodynamic profiles of the ambient air. We choose drop sondes representative of the atmospheric state close to each identified cloud, by using the following criteria:

- The release time of the drop-sonde needs to be not earlier and not later than $3\,\mathrm{h}$ of the cloud measurement time by the ATR.
- The drop sondes need to be in the same mesoscale feature and thus not further away than $100\,\mathrm{km}$ relative to the cloud measurement location.

This further reduces our number of rain clouds to 111.

2.2.2 Fits to observational data

We approximate the cloud base DSD and the thermodynamic profiles by analytic functions. This allows comparability to other studies, which use similar approximations (Sarkar et al., 2023; Seifert, 2008). Especially, bulk models need an analytic form of the DSD. With our approach, we allow bulk and bin schemes to also use our model initialisation data. It further reduces the degrees of freedom in our setup.

Droplet Size Distribution (DSD)

A common way to approximate the size distribution of either aerosols or cloud droplets is the use of a log normal distribution (Lohmann et al., 2016). For rain drop size distributions, it is common to use a gamma distribution (Marshall & Palmer, 1948; Naumann & Seifert, 2016; Ulbrich, 1983) but also log-normal distributions can be used Feingold and Levin, 1986. We also use a log-normal distribution to omit disproportionately large values at the low end of the radii scale (high probability densities near zero). We separate the DSD into a cloud and rain regime, which are divided by a droplet radius of $45\ \mu\mathrm{m}$. This is in-between the $40\ \mu\mathrm{m}$ radius chosen in the bulk scheme by Seifert and Beheng, 2001 and the $50\ \mu\mathrm{m}$ radius chosen in Bony et al., 2022 (based on the AMS glossary definition of cloud droplets). The bimodal log normal distribution for the whole DSD $N(r)$, is therefore the sum of the cloud droplet distribution $N_{cloud}(r)$ and the rain droplet distribution $N_{rain}(r)$ (Equation (1a)). Both follow the log normal distribution $L(r)$ given in Equation (1b) (Lohmann et al., 2016). There, $\tilde{\mu} = \ln \mu_g$ with μ_g denoting the geometric mean of the distribution and $\tilde{\sigma} = \ln \sigma_g$ with σ_g as the geometric standard deviation of the distribution. The fitted DSDs for all clouds can be seen as grey lines in Figure S2.

$$N(r) = N_{cloud}(r) + N_{rain}(r) \tag{1a}$$

$$L(r) = \frac{N_a}{\sqrt{2\pi}\tilde{\sigma}} \exp\left(-\frac{(\ln r - \tilde{\mu})^2}{2\tilde{\sigma}^2}\right) \quad \text{for } r > 0 \tag{1b}$$

Thermodynamics

For the 1D rainshaft model, we supply the profiles of specific humidity and air temperature. Usually, linear fits for the thermodynamic profiles are performed (Sarkar et al., 2023; Seifert, 2008). We distinguish the sub cloud layer and the cloud layer and apply a linear regression for each of them based on Equation (2). The height above the surface is h and the surface value of any thermodynamic variable is f_0. The vertical gradient/lapse rate of a thermodynamic variable is split at the cloud base height, h_{cb}, into the gradient in the sub cloud layer, m_{sc}, and the cloud layer gradient, m_c. For a consistent cloud base height, we first fit h_{cb} and keep it fixed for all thermodynamic variables while fitting the other free parameters (f_0, m_{sc} and m_c).

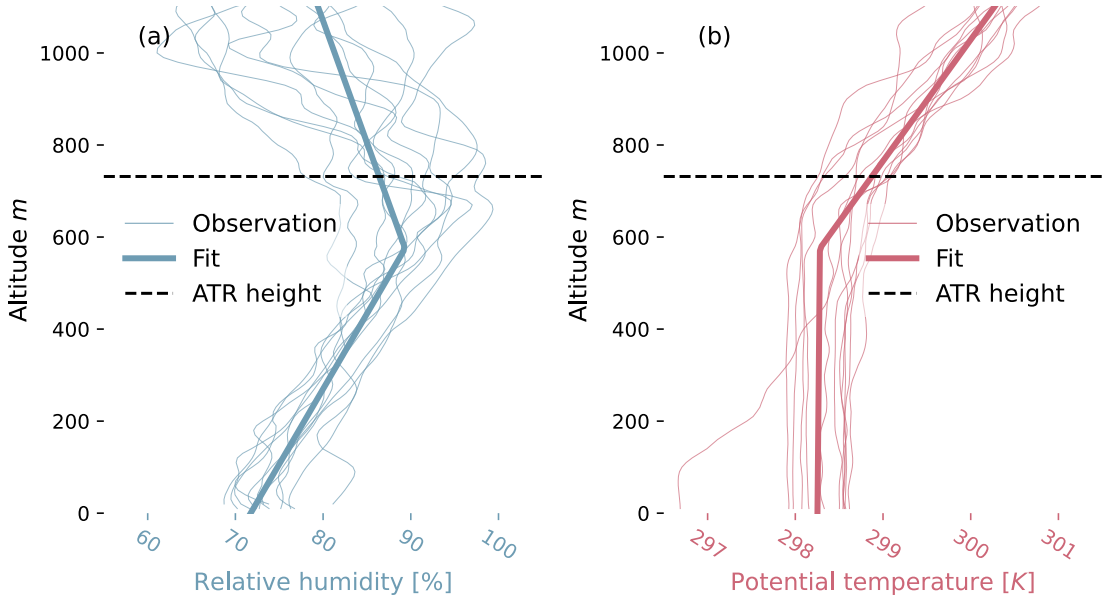

Figure 2: Relative humidity (a) and potential temperature (b) profiles against altitude for an arbitrary cloud (ID 142). Observations from related individual drop sondes as thin lines and analytic fits based on Equation (2) as thick lines. The dashed black line indicates measurement height of the ATR used as cloud base.

$$f(h) = \begin{cases} f_0 + m_{sc} \cdot h & \text{if } h \leq h_{cb} \\ f_0 + m_{sc} \cdot h_{cb} + m_c \cdot (h - h_{cb}) & \text{if } h > h_{cb} \end{cases} \tag{2}$$

For an arbitrarily selected cloud (ID 142), the drop sonde measurements and the fitted profiles of relative humidity and potential temperature can be seen in Figure 2. The 13 dropsonde profiles related to this cloud are shown as thin vertical profiles and show a similar vertical structure. The dropsonde profiles do not indicate saturation in the cloud layer, which contradicts what is expected. It is most likely because the drop sondes sampled the air outside of clouds. The relative humidity profiles for all individual clouds are shown in Figure 3. None of the profiles shows saturation near the cloud base, but the profiles span a realistic range of surface values and vertical gradients. The profiles are also realistic, because they are fully sub saturated.

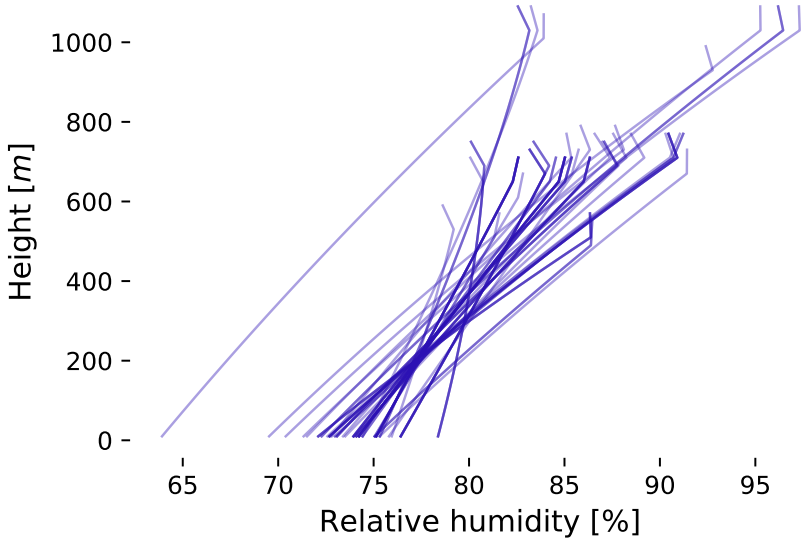

Figure 3: Relative humidity profiles for all clouds, which we use as model input. Each profiles correspond to an individual cloud. The top end of the profiles marks the height of the cloud layer and is approximately the height of the ATR measurement.

2.3 Model setup

2.3.1 Setup of the Super-Droplet-Model CLEO

For this study, we use version `v0.21.0` of the novel Super-Droplet-Model CLEO capable of simulating many microphysical processes in warm clouds (Bayley, 2024b; Bayley et al., n.d.). In contrast to many other Super-Droplet-Model and bin-schemes and nearly all bulk-schemes, it is not only capable to simulate the collisional coalescence of droplets, but also their collisional breakup. In order to model droplet-droplet interaction, probabilistic approaches for the collision outcomes are used (Bayley et al., n.d.; Shima et al., 2009). Further detail on how CLEO models these processes, can be found in Bayley et al., n.d. and CLEOs online Wiki (Bayley, 2024a). We do not use CLEOs novel capability to be run with large domain sizes of $O(100\,\mathrm{km})$, allowing it to be coupled to global storm resolving models.

Below, we describe which microphysical setups we use in our configuration of CLEO:

- Terminal velocity: `RogersGKTerminalVelocity` where the formula is based on the adaption of Rogers et al., 1993 from Gunn and Kinzer, 1949.
- Condensation and Evaporation: Follows the ordinary differential equation described by the Köhler Theory (Köhler, 1936; Rogers & Yau, 1989).

- Collision: We use the `LongHydroProb` setup for the efficiency of collection, which follows Simmel et al., 2002 based on Long, 1974. It defines the probability of the collision of two droplets.
- Coalescence: Using the`LongHydroProb` kernel also defines the probability of coalescence.
- Coalescence, Breakup and Rebound: We use `TSCoalBuReFlag` to define the probabilities for the three collision outcomes. It depends on the ratio between collision kinetic energy and the surface tension energy of the droplets and follows the findings by Straub et al., 2010. For the breakup event, we prescribe a fixed number of fragments.

Setup	Terminal velocity	Evaporation Condensation	Collision Coalescence	Collision Breakup + Rebound
Condensation/Evaporation (CE)	Yes	Yes	X	X
Coalescence (COAL)	Yes	Yes	Yes	X
CoalBuRe few fragments (CBR_F)	Yes	Yes	Yes	Yes (5)
CoalBuRe many fragments (CBR_M)	Yes	Yes	Yes	Yes (125)

Table 1: Individual microphysical model setups, which we use in this study. For the breakup, we prescribe a fixed number of fragments produced per breakup event, given in brackets.

We use four microphysical setups in this study, whose resolved microphysical processes are summarized in Table 1. All setups simulate terminal velocity and evaporation and condensation. The Coalescence (COAL) setup also incorporates collisional coalescence of droplets. The CoalBuRe few fragments (CBR_F) and CoalBuRe many fragments (CBR_M) setups include collisional coalescence, rebound and breakup, whereas the number of fragments per breakup event for the CBR_M setup is 125 and five for the CBR_F setup.

We divide our 1D rainshaft model at cloud base height into a cloud layer and a sub cloud layer. The cloud layer is $100\,\mathrm{m}$ thick and the sub cloud layer consists of a varying number of $20\,\mathrm{m}$ thick gridboxes. We use the ATR flight height to approximate the cloud base height. Other than Seifert, 2008, we do not simulate the evolution of a cloud over time, but analyse the snapshot in the cloud's lifecycle for during which the DSD was measured on the ATR aircraft. Therefore, we keep the cloud base DSD constant for the whole simulation period, for our model to reach a stationary state representing this snapshot of the sub cloud layer. The stationary state is reached, whenever the DSD is stationary in all gridboxes. We discuss

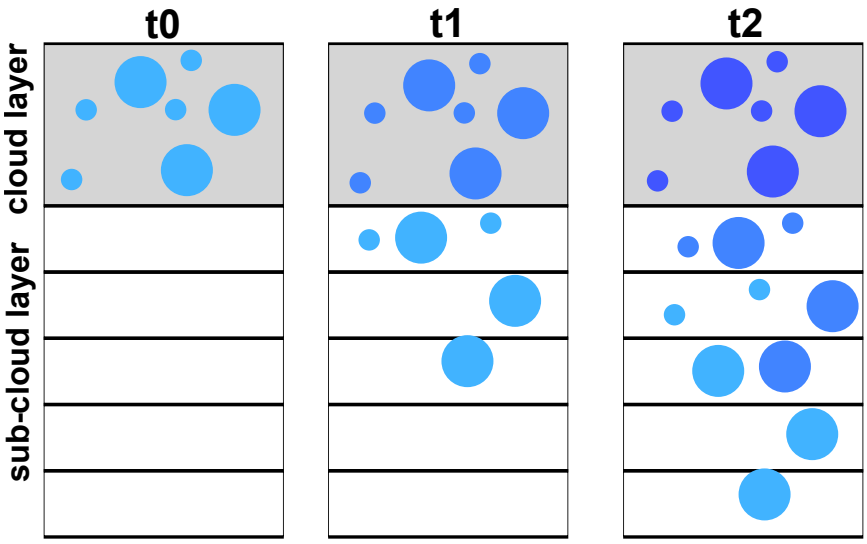

Figure 4: Illustration of our model setup over 2 model iterations. Circles as individual super-droplets, which fall into the sub cloud layer, with their size as the droplet radius. Darker colour represents a later spawning in the cloud layer. The DSD in the cloud layer is kept constant over the simulation time.

this in more detail in Section 3.1. A schematic of our setup can be seen in Figure 4, which illustrates the transition from the model initialisation towards the stationary state. In the stationary state, droplets of diverse size ranges are present in each gridbox of the domain, which enables droplet-droplet interaction across these diverse size ranges, as occurring in reality. Without a constant DSD in the cloud base, due to gravitational sorting, nearly no interaction between droplets of different size would be possible in the lower gridboxes (see Figure S3).

We initialise 2048 super-droplets with each motion time step of $2\,\mathrm{s}$ with radii from $0.1\,\mu\mathrm{m}$ to $1\,\mathrm{mm}$. The evolution of all super-droplets, which fall into the sub cloud layer within the motion time step, is further simulated. Super-droplets which do not reach the sub cloud layer are removed from the simulation [1]. New super-droplets spawn at each time step of the simulation. This makes the DSD below the initialisation gridbox (cloud layer) sensible to our prescribed motion time step. A longer time step allows more small droplets with lower terminal velocity to fall below the cloud base. We find our motion time step of $2\,\mathrm{s}$ to allow realistic concentration of droplets with radii from approximately $10\,\mu\mathrm{m}$ to $1\,\mathrm{mm}$ to reach the sub cloud layer. In the stationary state, all gridboxes contain more than 100 super-droplets, which we assume to be accurate enough to simulate all microphysical processes

[1] This could be a small droplet which was spawn in the top of the cloud layer, which does not fall fast enough to reach the cloud base, due to its low terminal velocity

sufficiently. A lower number of SDs showed enhanced variability of the stationary state.

For super-droplets precipitating in the surface gridbox, it is not possible to distinguish between evaporation and precipitation. Thus, we refer to the second-lowest gridbox, centred at centre $30\,\mathrm{m}$ height, as the surface. The highest sub cloud gridbox is also unsuitable because extensive amounts of drizzle can exist, which evaporate nearly completely in this layer. We refer to the second-highest gridbox in the sub cloud layer as cloud base, with its centre at $30\,\mathrm{m}$ beneath the cloud layer. We mainly use this notation in Section 3.5. The difference between cloud layer and cloud base LWC is neglectable, but their DSDs differ (Figure S2).

2.3.2 Calculation of metrics

The output from CLEO is a Lagrangian output, giving data for each of the N super-droplets along their trajectories. But the Eulerian form is preferable because it describes the state of the sub cloud layer as modelled in most operating models and other microphysical schemes and how it is observed in reality. Therefore, a transformation from the Lagrangian to the Eulerian state in necessary and describe further down.

A few notes on our notation:

- i : Index for individual super-droplet. For N super-droplets, $i \in [1, N]$
- t : Time of the simulation
- g : Gridbox index for the domain gridboxes, 1 for the surface and G for the cloud layer.
- b : Individual radius bin for a number of log-spaced radii bins.
- Δt : The modelling time step (we use $2\,\mathrm{s}$).
- We denote a selection of an individual super-droplet with $[i]$. The dependency of a variable on a dimension is denoted as $(...)$, e.g. on time (t).

Each super-droplet with index i is present in the domain from its time of initialization, $t_s[i]$, until the time when it leaves the domain, $t_e[i]$. It has time varying attributes radius, $r[i](t)$ and total mass, $m[i](t)$, within its existing time $t \in [t_s[i], t_e[i]]$. Its altitude, $z[i](t)$, is related to the gridbox which it is present in, $h[i](t)$. Further, it represents a number of real droplets, which is given as its multiplicity, $\xi[i](t)$. The total mass of real droplets, which a super-droplet represents, is given by $m_{rep}[i](t) = m[i](t) \cdot \xi[i](t)$.

Lagrangian to Eulerian transformation ($L2E$)

We can transform a variable from a Lagrangian variable $x[i](t)$ as a function of time for each individual super-droplets to an Eulerian variable $x(t, g, b)$ as a function of time, gridbox and radius bin. All super-droplets which are in the same radius bin, b, and the same gridbox g, get binned together. We can then apply an operator OP like the summation $\sum_i$ over the set of selected super-droplets. This is expressed in Equation (3).

$$L2E\left[OP\right]\Big(x[i](t)\Big) : OP\Big(x[i](t)\Big) \quad \Big\{\forall\, i \mid h[i](t) = g \wedge r[i](t) \in b\Big\} \tag{3}$$

Liquid Water Content (LWC)

To calculate the LWC, we need to compute the total mass of liquid water represented by the super-droplets. We are interested in the Eulerian form to describe the state of the sub cloud layer, which we calculate by using the $L2E$ transformation (Equation (3)). We divide by the volume of a gridbox (V_g) to get the LWC in $\mathrm{kg\,m^{-3}}$.

$$LWC(t, g, b) = L2E\left[\sum_i\right]\left(\frac{m_{rep}[i](t)}{V_g}\right)$$

Precipitation

We define the precipitation as the amount of mass which leaves the surface gridbox ($g = 1$) over one simulation time step. For each super-droplet the precipitation ($p[i]$) it produces is equivalent to its mass at its last individual time step before leaving the domain, $m_{rep}[i](t = t_e[i])$. This does not take the evaporation during this time step into account, but we argue that this effect is neglectable. The total precipitation rate is then divided by the modelling time step.

$$P(t, b) = \sum_i \frac{p[i]}{\Delta t} \quad \Big\{\forall\, i \mid t_e[i] = t \wedge r[i](t_e[i]) \in b \wedge h[i](t_e[i]) = 1\Big\}$$

Latent cooling (LC)

Whenever we are not interested in the radii dependency of the latent cooling (LC), we use the Lagrangian output from CLEO, which monitors the evaporated mass per simulation iteration, $\Delta m_{evp}(t, g)$. We use the specific latent heat of water $L_V = 2265\mathrm{kJ\,kg^{-1}}$ to calculate the latent cooling. Note that the minus sign in the equation is needed to get the latent cooling and not the latent heating.

$$LC(t, g) = -\frac{\Delta m_{evp}(t, g)}{\Delta t} \cdot L_V$$

Latent cooling dependent on the radius

For the latent cooling for individual droplet radii bins, we used a Lagrangian approach to first calculate the mass change for each super-droplet at a time step as the difference to the previous time step.

$$\Delta m_{rep}[i](t) = m_{rep}[i](t) - m_{rep}[i](t-1)$$

It is very important to notice that this value includes not only the change in mass due to evaporation, but also the change in multiplicity, $\xi[i]$. Both can change by droplet-droplet interaction like coalescence or breakup. But the total mass of all super-droplets can only change by evaporation. Thus, the integrated quantity is still a measure of evaporation. We transform the mass change again into an Eulerian variable with dependency on time, gridbox and radius bin, by using the $L2E$ transformation (Equation (3)).

$$LC(t, g, b) = L2E\left[\sum_i\right]\left(-\frac{\Delta m_{rep}[i](t)}{\Delta t} \cdot L_V\right)$$

Column integrated latent cooling (LC_CI)

To get the column integrated latent cooling, we integrate the LC over the gridboxes and multiply by each gridbox thickness $\Delta h(g)$.

$$LC_{CI}(t, b) = \sum_g LC(t, g, b) \cdot \Delta h(g)$$

Droplet evaporated fraction

Each super-droplet evaporates a fraction of its mass per model time step, F_{sd}. The units are then given in Δt^{-1} or using percentage values $\%\Delta t^{-1}$. The value is identical for the real droplets represented by the super-droplet. A super-droplet which evaporates completely over one modelling time step has $F_{sd} = 100\%\Delta t^{-1}$. We derive the Eulerian form using $L2E$.

$$F_{sd}[i](t) = \frac{\Delta m[i]}{m[i]}(t)$$
$$F(t,g,b) = L2E\left[\sum_i\right]\left(\frac{\Delta m[i]}{m[i]}(t)\right)$$

Calculation of mean and SEM

We denote the mean of a variable x over the time of the stationary state as $\overline{x}^{(t)}$ and over all clouds as $\overline{x}^{(c)}$. In order to estimate the total mean over the stationary state over all clouds, we firstly compute mean over time and then over all clouds $\overline{x}^{(t,c)}$. We use standard error propagation for the calculation of the related errors and calculate the (SEM) following the Central Limit Theorem.

3 Results and Discussion

3.1 Stationary state and realistic validation

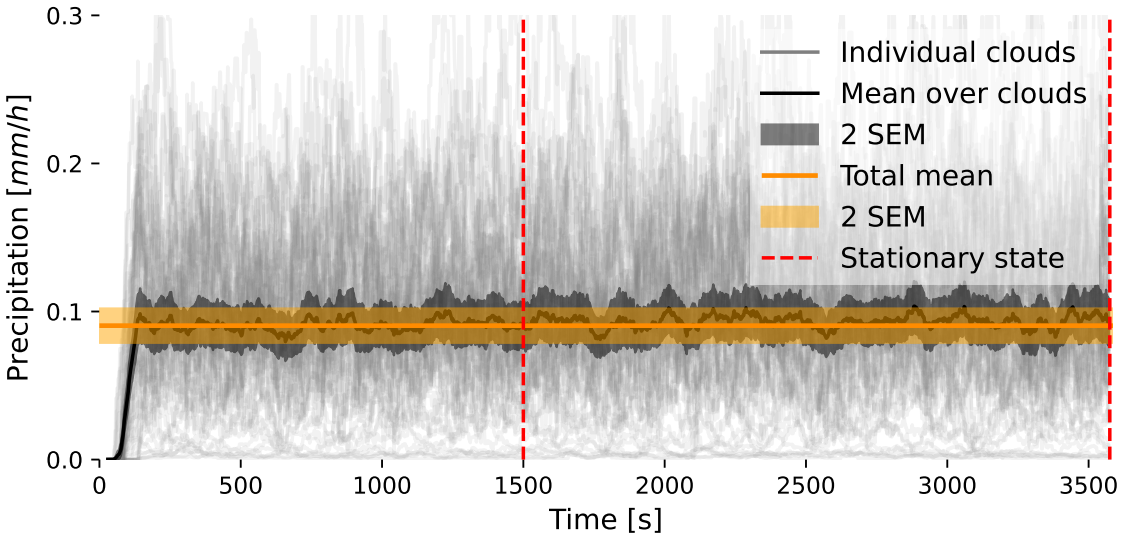

Figure 5: Temporal evolution of precipitation (P) in the Condensation/Evaporation (CE) simulations with applied rolling mean of $60\,\mathrm{s}$. Thin grey lines for each individual cloud simulation. Black line as the mean over all clouds per timestep ($\overline{P}^{(c)}(t)$) with shading as double SEM. Red vertical dashed lines mark the time range identified as stationary state and used for all temporal mean calculations. Orange horizontal line as mean over temporal mean of individual clouds $\overline{P}^{(t,c)}$ and orange shading as double SEM (mean by time and then over clouds).

In a first step, we aim to understand how realistic the results from our simulations are. For this, we have a closer look into the Condensation/Evaporation (CE) setup.

The precipitation rates we simulate should be interpreted as the precipitation intensity below a cumulus cloud in the winter trades. We use a rolling mean of $60\,\mathrm{s}$ to smooth out the impact of an individual super-droplets leaving the domain. This gives us a relatively smooth temporal evolution of precipitation for each individual cloud. The spin up of the model is

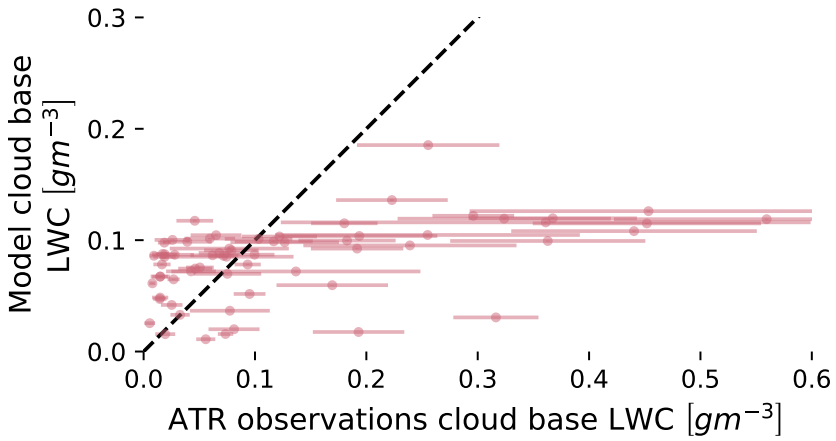

Figure 6: Comparison of LWC between observations taken on the ATR flights and our model initialization. We calculate mean and SEM for ATR observations over all measurements within individual clouds and for our model initialisation over the stationary state. Black dashed line as 1:1 line.

identified by the onset of precipitation at the surface for all clouds and the inter-cloud mean and SEM which are shown as thick black line and shading in Figure 5). The smoothed precipitation shows a saturation with constant variance after approximately $200\,\mathrm{s}$, which indicates that the model reached its stationary state. We can therefore safely approximate the stationary state of a variable by calculating the mean over the time range from $1500\,\mathrm{s}$ until the end of the simulation. We note, that individual super-droplets are the source of precipitation, explaining the high variance of the precipitation rates for individual clouds (see Figure S4).

The stationary state of surface precipitation for all clouds ranges from very low precipitation $\leq 0.01\,\mathrm{mm\,h^{-1}}$ to $0.2\,\mathrm{mm\,h^{-1}}$, and the mean over all stationary states is $0.093 \pm 0.006\,\mathrm{mm\,h^{-1}}$ (Figure S5). These precipitation intensities are lower compared to the observational based climatological rates of $0.41\,\mathrm{mm\,h^{-1}}$ to $1.45\,\mathrm{mm\,h^{-1}}$ within cold pools passing over the Barbados Cloud Observatory, identified by Vogel et al., 2021.

We find a nearly perfect correlation ($R = 0.98$) of the cloud base LWC to the precipitation rates (Figure S6). With our initialized LWC at cloud base is too low compared to the observations measured by the ATR Figure 6, we can therefore most likely explain our underestimation of precipitation. The LWC derived from the ATR measurements shows values exceeding $0.2\,\mathrm{g\,m^{-3}}$. The main reason for our underestimation of cloud base LWC is that the fit of an analytic form of the DSD underestimates the concentration of larger rain droplets. It is in general challenging to fit the DSD analytically while simultaneously preserving the LWC.

We expect the precipitation intensity to be more realistic after adjusting our LWC, which we leave for future work. Still, the surface precipitation and LWC are in a reasonably realistic range compared to Vogel et al., 2021 and Sarkar et al., 2023. Sarkar et al., 2023 used similar values of LWC in some of their simulations.

Within the stationary state, it is crucial that the DSD shows stationary properties in each gridbox. The surface gridbox is the last gridbox to reach stationary state, which occurs around approximately $700\,\mathrm{s}$ for most clouds, which is well before the chosen $1500\,\mathrm{s}$ time limit (Figure 5). The temporal evolution of the real droplet number concentration against log-spaced radii bins for an arbitrary cloud (cloud ID 295) can be seen in Figure S7, supporting our previous statement.

3.2 Rain evaporation and latent cooling profiles

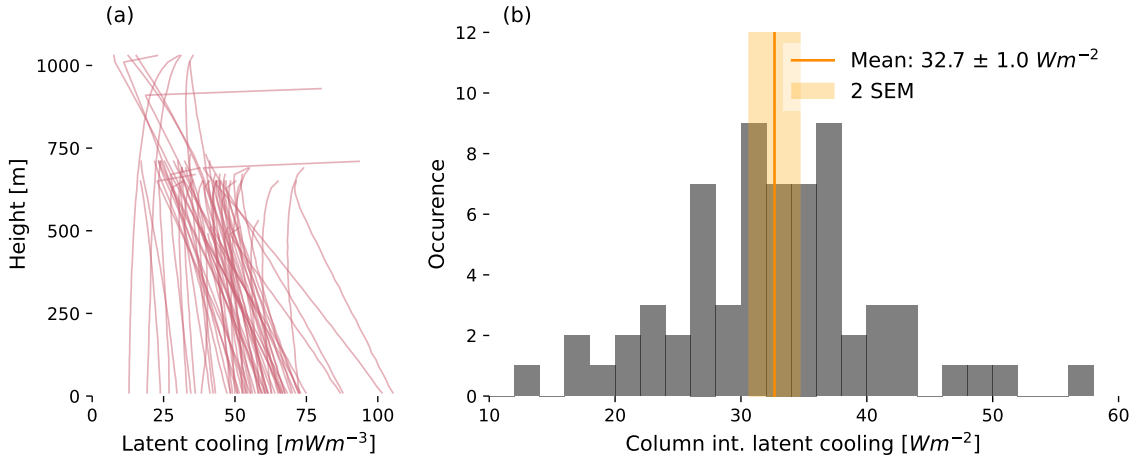

Figure 7: (a): Vertical profiles of latent cooling (LC) for all simulated clouds. Each of the clouds has an individual cloud base height. (b): Histogram of stationary state column integrated latent cooling (LC_{CI}) for all clouds. Mean and double SEM are shown as orange line and shading. Mean calculated over stationary state first, then over all clouds $\overline{LC_{CI}}^{(t,c)}$.

Figure 7 (a) shows the vertical profiles of LC for all cloud simulations in the Condensation/Evaporation (CE) setup, with a wide inter-cloud spread ranging from $10\,\mathrm{mW\,m^{-3}}$ to $110\,\mathrm{mW\,m^{-3}}$. For most clouds, stronger latent cooling near the surface can be seen (bottom-heavy), but a few profiles show more latent cooling beneath the cloud base than at the surface (top-heavy). We can further identify a similar slope of the vertical profiles for many clouds, especially for clouds with a cloud base height of approximately $700\,\mathrm{m}$. The reason

could be the similar relative humidity profiles prescribed for the columns, which we further discuss in Section 3.3. The very intense LC near cloud base for some clouds might be an artifact of our model setup and the prescribed low relative humidity (sub-saturation). For some DSDs, large amounts of small droplets with radii below $45\,\mu\mathrm{m}$ (cloud droplets) can fall into the sub cloud layer and evaporate nearly completely in its top most layer, due to their low terminal velocity. Fixing the issue of strong sub saturation near cloud base could solve this artifact. It also shows that drizzle needs to be carefully considered, especially because it can be strongly affected vertical structure of LC.

The values of column integrated latent cooling (LC_{CI}) range from $12\,\mathrm{W\,m^{-2}}$ to $58\,\mathrm{W\,m^{-2}}$ with a mean of $32.7 \pm 1.0\,\mathrm{W\,m^{-2}}$ (Figure 7 b). These values are at the lower end of the results given by Sarkar et al., 2023 of $15\,\mathrm{W\,m^{-2}}$ to $352\,\mathrm{W\,m^{-2}}$ and the values from the radar retrieval of deeper continental convection with values of $190\,\mathrm{W\,m^{-2}}$ identified by Tridon et al., 2017. This is in line with our underestimation of the LWC at cloud base, as explained previously. On the other hand, our overall estimation on the fraction of rain which evaporates is much lower, with a mean of $7.1 \pm 0.9\,\%$ compared to approximately $63\,\%$ identified by Sarkar et al., 2023 (Figure S8). We also find more bottom-heavy profiles, whereas Sarkar et al., 2023 identified more top-heavy profiles. These differences are most likely due to our DSDs being more shifted towards larger droplet radii compared to those of Sarkar et al., 2023. Having more large droplets within a distribution of the same LWC, decreases the total surface area of all droplets and thus leads to lower evaporation rates in a given time. Small droplet also have a lower terminal velocity and thus evaporate closer beneath the cloud base leading to more top-heavy profiles. We discuss the impact of the droplet radius on the evaporation rates and latent cooling further in Section 3.4.

3.3 Influence of environmental state and cloud properties on rain evaporation

We want to understand the influence of cloud properties and the thermodynamics on rain evaporation better, by comparing the LC within each gridbox to the LWC and relative humidity for each cloud, which is shown in Figure 8. We can identify LC to strongly depend on the LWC of the gridbox, with higher LWC leading to stronger LC to a first approximation. The LWC reduces towards the surface due to the evaporation of droplets. Nevertheless, the

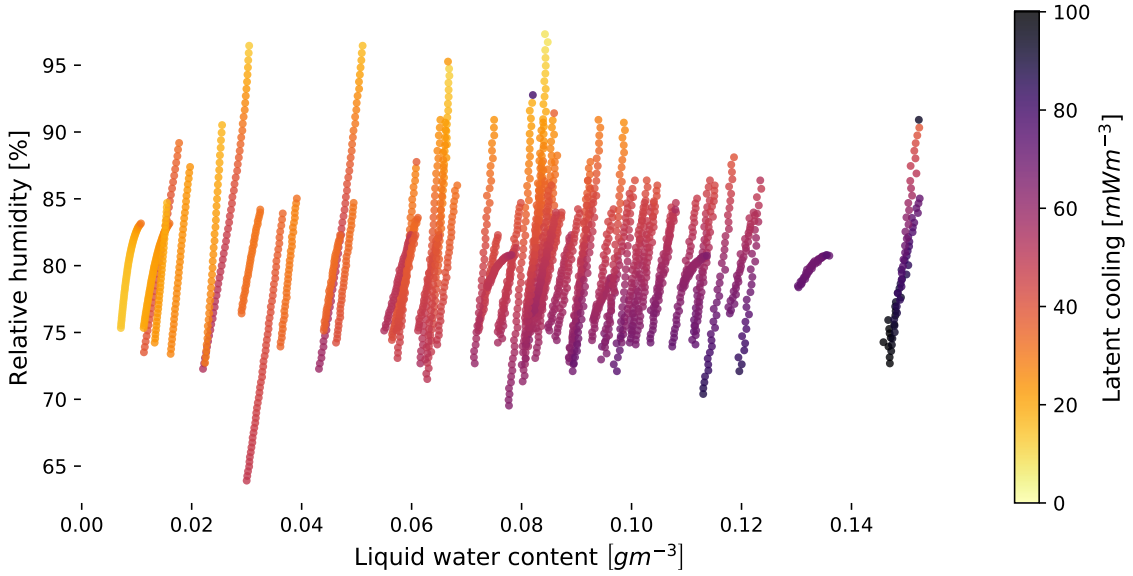

Figure 8: Scatter of stationary state LC against LWC and relative humidity for all clouds. Each dot represents the values for one gridbox and an individual cloud, and is coloured by the LC. Individual clouds as lines of dots from top (cloud base) to bottom (surface).

LC increases for most clouds towards the surface. This is in line with the lower relative humidity near the surface. The LWC in the cloud layer seems to constrain the mean strength of LC in the sub cloud layer, whereas the relative humidity profiles seem to modulate the shape of the vertical profile by enhancing the LC towards the surface.

To disentangle the impacts of cloud-base LWC and the relative humidity, Figure 9 compares the column integrated latent cooling (LC_{CI}) with the LWC at cloud base and the vertical gradients of LC with those of relative humidity for each cloud. The cloud base LWC can explain approximately $50\,\%$ of the LC_{CI} inter-cloud variability with a Pearson correlation coefficient of $R = 0.71$. The correlation indicates that more LWC in the cloud layer leads to stronger LC. The prescribed cloud base height does not correlate well with the LC_{CI} with $R = 0.16$ (Figure S10). Nevertheless, higher cloud bases can have similar LC_{CI} values even for profiles of lower LC, due to their deeper sub cloud layer.
The vertical gradients of relative humidity and LC correlate well with a Pearson correlation coefficient of $R = -0.82$, explaining approximately $67\,\%$ of the inter-cloud variability. A stronger increase of relative humidity with height, leads to more latent cooling near the surface than close to the cloud base. The vertical gradient of LC does not depend strongly on the cloud base LWC ($R = 0.60$) (Figure S9 (c)). We neither find a strong correlation between the surface relative humidity and the LC_{CI} ($R = -0.16$) nor with the LC vertical

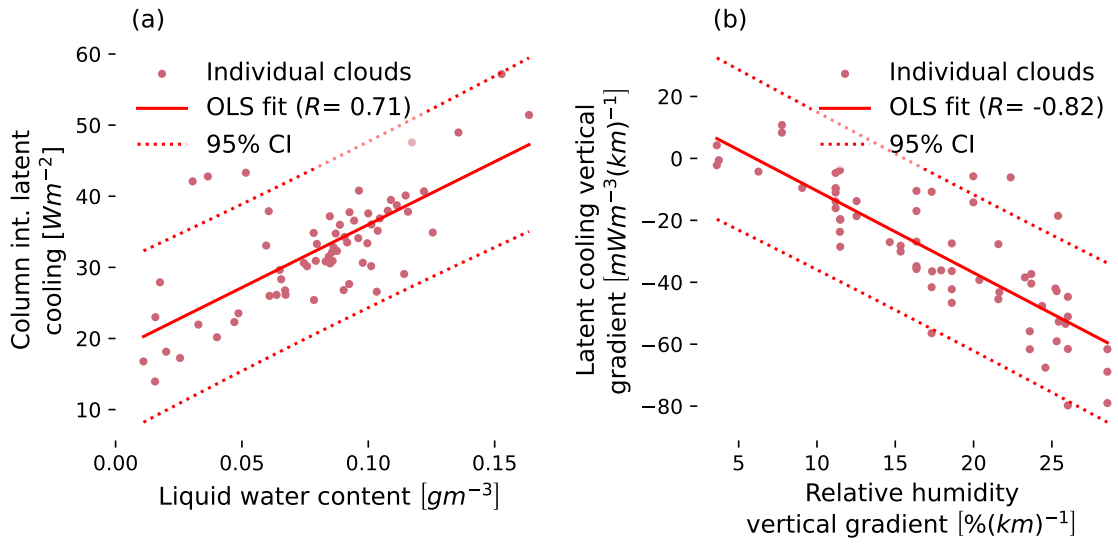

Figure 9: *Left*: Scatter of the column integrated latent cooling against the LWC in the cloud layer. Each dot represents an individual cloud. Solid red line as linear regression with corresponding $95\,\%$ confidence interval (CI) based on Ordinary-Least-Square (OLS) method. The Pearson-Correlation-Coefficient (R) shown in the legend. *Right*: As on the left but for the vertical gradients of LC and relative humidity profiles. We compute a vertical gradient as the slope of a linear regression of the stationary state profiles.

gradient ($R = 0.46$) (Figure S10). This differs from the findings by Sarkar et al., 2023 who identified the surface relative humidity to modify the latent cooling. The reason could be, that we do not prescribe saturation of air at cloud base while they did. Therefore, our gradient of relative humidity can alter more independently of the surface values. If we modify the fit for the thermodynamic profiles, we could expect the surface relative humidity to play a more prominent role, while the vertical gradient of relative humidity would be directly dependent on the surface humidity values.

To publish our results in a scientific journal, we will adjust the LWC of our fitted DSD to match the observations better, which most likely results in stronger evaporation and latent cooling. Nevertheless, due to the high correlation of LC to LWC, we expect our findings to be qualitative similar. Simultaneously, we plan to refine our thermodynamic profiles by prescribing the cloud base relative humidity to either $100\,\%$ or the measurements taken onboard of the ATR aircraft (Bony et al., 2022). A better vertical gradient could be retrieved by fitting a simple linear regression to measurement between $200\,\mathrm{m}$ to $500\,\mathrm{m}$ altitude.

3.4 Influence of droplet radius on rain evaporation

The main difference remaining between each individual cloud is the distribution of the LWC across the individual droplet radii, in other words, the mass size distribution (MSD) at cloud base. To understand the influence of the droplet radius, we will have a look at the LC, DSD and mass size distribution (MSD) dependency on droplet radii for all clouds simulated in the CE setup at the cloud base and the surface (Figure 10).

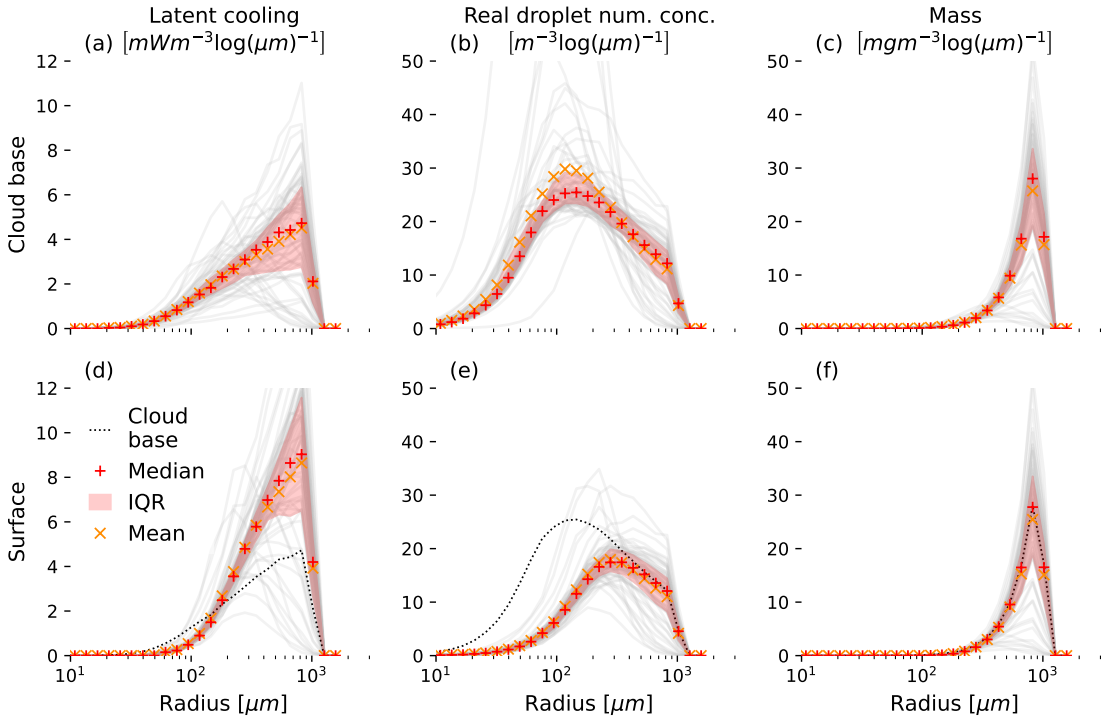

Figure 10: Shown are Latent cooling (LC) (a,d), the real droplet number concentration (as the DSD) (b,e) and the MSD (c,f) for the CE setup at cloud base (a-c) and at the surface (d-f). Thin grey lines are the stationary states of individual clouds. Red crossed indicate the median with red shading as the Inter Quartile Range (IQR) ($25\,\%$ to $75\,\%$ interval). Orange crosses indicate inter-cloud mean values. For the surface (d-f), the dashed black line indicates the median from the cloud base.

The vertical change of the DSD is quite prominent for droplets with radii of approximately $100\,\mu\mathrm{m}$. These droplets evaporate strongly, and their number concentration reduces by approximately $75\,\%$ comparing the cloud base with the surface (Figure 10 b and c). The number concentration and the mass of droplets with radii between $500\,\mu\mathrm{m}$ to $1\,\mathrm{mm}$ does not change substantially from the cloud base towards the surface. Their induced latent cooling is enhanced near the surface due to lower relative humidity. In general, the distribution

gets narrower and shifts towards larger radii, which is in line with the findings by Sarkar et al., 2023 and Seifert, 2008.

The main contribution of latent cooling is produced by the larger droplets with radii of approximately $1\,\mathrm{mm}$, because they contain most of the mass. Their latent cooling rates are approximately $5\,\mathrm{mW\,m^{-3}}$ at cloud base and $9\,\mathrm{mW\,m^{-3}}$ at the surface (Figure 10 a and c). The dependency of the latent cooling on droplet radius is not fully explained by the shape of the MSD, which shows an exponential like shape with a cut of on the upper radii range in the log-linear space (Figure 10 c and f). The real droplet concentration for the large droplets nevertheless shows a log-normal like distribution with a flat maximum around $100\,\mu\mathrm{m}$ radius (Figure 10 b and e). It is the mixture of both, which can describe the dependency of latent cooling on the droplet radii. the reason lays in the fundamental dependency of evaporation on droplet sizes.

In Chapter 1 we discussed briefly how the radius of a droplet changes its evaporation behaviour. Large droplets have a larger surface area, allowing them to evaporate more mass than small droplets in a given time, whereas small droplets evaporate a larger fraction of their mass in a given time, due to their larger surface area to mass ratio. A set of small droplets, containing the same amount of water like a set of large ones, evaporates a larger fraction of its mass in a given time. They have a higher evaporation efficiency [1]. Figure 11 shows the evaporated fraction (measure for evaporation efficiency) of droplets in the surface gridbox over one modelling time step of $2\,\mathrm{s}$, Δt. Droplets with radii below $10\,\mu\mathrm{m}$ evaporate nearly completely over one modelling time step ($100\,\%$), whereas droplets above $100\,\mu\mathrm{m}$ radius evaporate only approximately $1\,\%$ of their mass per modelling time step, which is consistent over all clouds, highlighting the physical origin of this effect. Small droplets evaporate more efficiently, which has

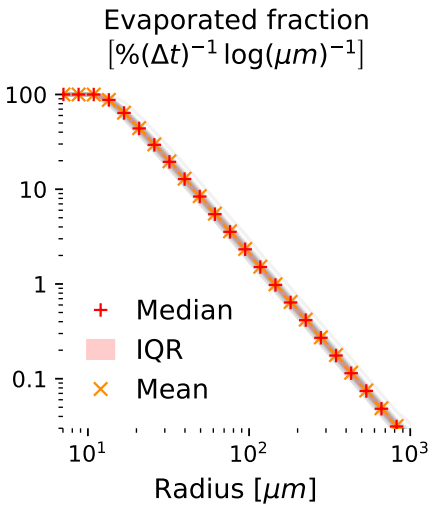

Figure 11: Evaporated fraction of droplet mass within one modelling time step of $2\,\mathrm{s}$, Δt, against droplet radius for CE setup in the surface gridbox. Evaporated fraction of individual droplet as $\frac{\Delta m[i]}{m[i]}\,(t)$, per modelling time step $\left[\%\Delta t^{-1}\right]$. Lines, shading, and markers as in Figure 10.

[1] This should not be confused with the rain evaporated fraction for cloud base LWC. Therefore, we use the term evaporation efficiency to refer to the evaporation fraction of individual droplets or a set of droplets within a given time.

direct impact on how microphysical processes influence the evaporation and latent cooling, because they alter the shape of the DSD and MSD.

3.5 Influence of microphysical processes on rain evaporation

Previous observationally-constrained rain shaft models mainly used a microphysical bin-schemes and considered evaporation of rain droplets but neglected the droplet collisional on rain evaporation. Collisions of droplets can either lead to collision-coalescence, break up into smaller fragments or a rebound of the droplets. Because evaporation efficiency depends strongly on the droplet radii range, these processes can alter the evaporation rate by transferring mass from a set of droplets to another set of droplets with different radii. The individual microphysical processes influence the MSD and the LC in the following manners:

- *Coalescence*: Shift of mass from smaller to larger droplet radii and reduction of the total number concentration of droplets. Because larger droplets evaporate less efficiently, we assume the coalescence to reduce evaporation and latent cooling overall.
- *Breakup*: Shift of mass from larger to smaller droplet radii and an increase in the number of droplets. The size of the new droplets depends on the breakup type, but can be simplified by the number of fragments (new small droplets) which are created. Regardless of this, the effect of breakup should yield a higher evaporation rate and latent cooling, as the shift of mass is opposite to the coalescence effect.
- *Rebound*: No effect on the MSD. It reduces coalescence slightly more than breakup and thus has an indirect effect on evaporation and latent cooling, which should be neglectable.

The latent cooling profiles for all clouds with the same cloud base height of $650\,\mathrm{m}$ simulated with the four microphysical setups are shown in Figure 12. Individual clouds can be seen as thin lines for all setups in Figure 12 (b-e). We identify the inter-cloud spread within a single setup to be larger than the difference in the mean profiles between all setups, except for the CoalBuRe many fragments ($\mathrm{CBR_M}$). For the $\mathrm{CBR_M}$ setup, we prescribe an unrealistically high amount of fragments 125 and should be understood as an upper bound on the effect of breakup on the evaporation and latent cooling. This setup creates very small droplets with

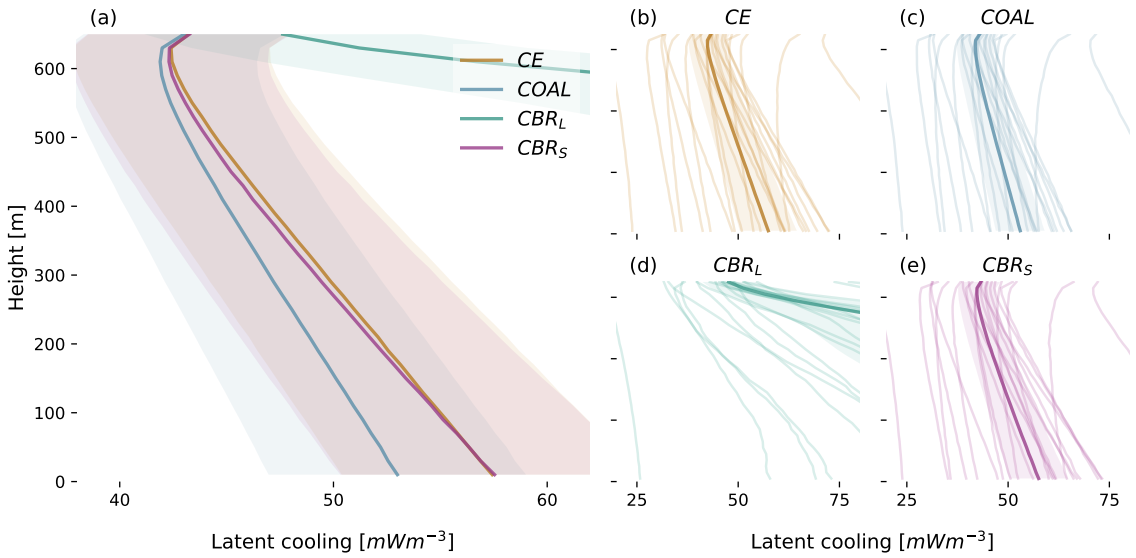

Figure 12: Latent cooling profile of the stationary state for all clouds as thin lines for each model setup CE (b), COAL (c), CBR$_F$ (d), CBR$_M$ (e). The inter-cloud mean for each setup shown as darker thick line with darker shading for the double SEM for all setups (b-e). Only clouds with the same cloud base height at $650\,\mathrm{m}$ are shown. Comparison of all inter-cloud mean latent cooling profiles ($\overline{LC}^{(t,c)}$) are shown in panel (a).

radii of approximately $100\,\mu\mathrm{m}$ in the sub cloud layer, increasing the evaporation efficiency strongly. Thus, the CBR$_M$ setup produces approximately four times stronger LC values than the other three setups (see also Figure S11).

The three realistic setups, CE (b), COAL (c), CBR$_F$ (e) show mean LC values of approximately $43\,\mathrm{mW\,m^{-3}}$ at cloud base and have similar vertical profiles. The COAL setup shows the lowest values of surface LC with $53\,\mathrm{mW\,m^{-3}}$ and the CE setup the highest with $58\,\mathrm{mW\,m^{-3}}$. The SEM of the stationary state of individual clouds is nearly neglectable compared to the inter-cloud spread, and the inter-cloud spread is much larger than the inter-setup differences. Thus, we find the microphysics to have only a small impact on the overall latent cooling during EUREC^{4}A.

Nevertheless, differences exist, particularly in vertical structure. We compare the microphysical setups for each cloud against the CE setup, which is shown in Figure 13. All clouds indicate a similar change for each microphysical setup. The mean differences between the microphysical setups are significant by more than their double SEMs (Figure 13 (a)). This gives us confidence that the microphysics do alter the vertical structure of the latent cooling due to their underlying effect on the DSD and MSD consistently across a large range of individual clouds. Qualitatively similar results can be seen using all clouds (Figure S12).

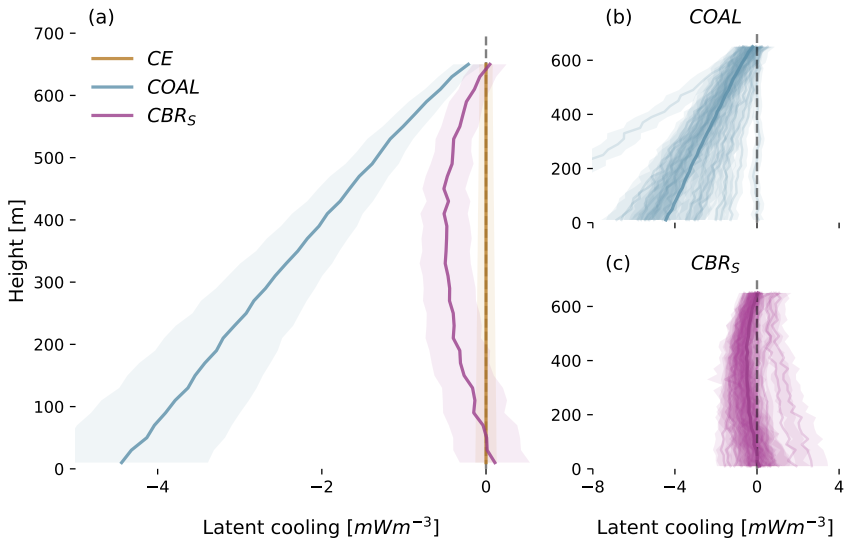

Figure 13: Similar to Figure 12, but here for the difference of the latent cooling profiles of the COAL (b), CBR_F (c) with the CE setup are shown. We calculate the difference for each individual cloud separately. The mean and SEM are then calculated across the set of clouds (with error propagation).

For the COAL setup, latent cooling is reduced throughout the column, with an increased reduction towards the surface (Figure 13 (b)). The reduction is $4.2\,\mathrm{mW\,m^{-3}}$ near the surface, a relative difference of approximately $10\,\%$ compared to the mean latent cooling of the CE setup. This can be explained by the coalescence of many small droplets into less large ones. The large droplets have a smaller surface area and thus evaporation is reduced, they evaporate less efficiently.

For the collision-coalescence-breakup and rebound cases with small fragments (CBR_F), we can see that this effect is weakened (Figure 13 (c)). The reduction of latent cooling is less compared to the COAL setups throughout the sub cloud layer and only slightly larger than the double SEM. The reduction in latent cooling by coalescence is counteracted by breakup, introducing smaller droplets into the sub cloud layer, which have a larger surface area, leading to more evaporation. Breakup increases evaporation efficiency. But it depends strongly on the number of breakup fragments. For the CBR_M setup with the higher number of fragments (125) even smaller droplets are created, and evaporation is much more enhanced (Figure S12 (d)). Further, we can identify the change to be non-linear along the vertical, which most likely is related to the lower relative humidity near the surface, enhancing the evaporation efficiency between small and large droplets. But more investigations are needed to understand this effect in more detail.

To better understand the effects of collisional droplet interaction, we look into the droplet

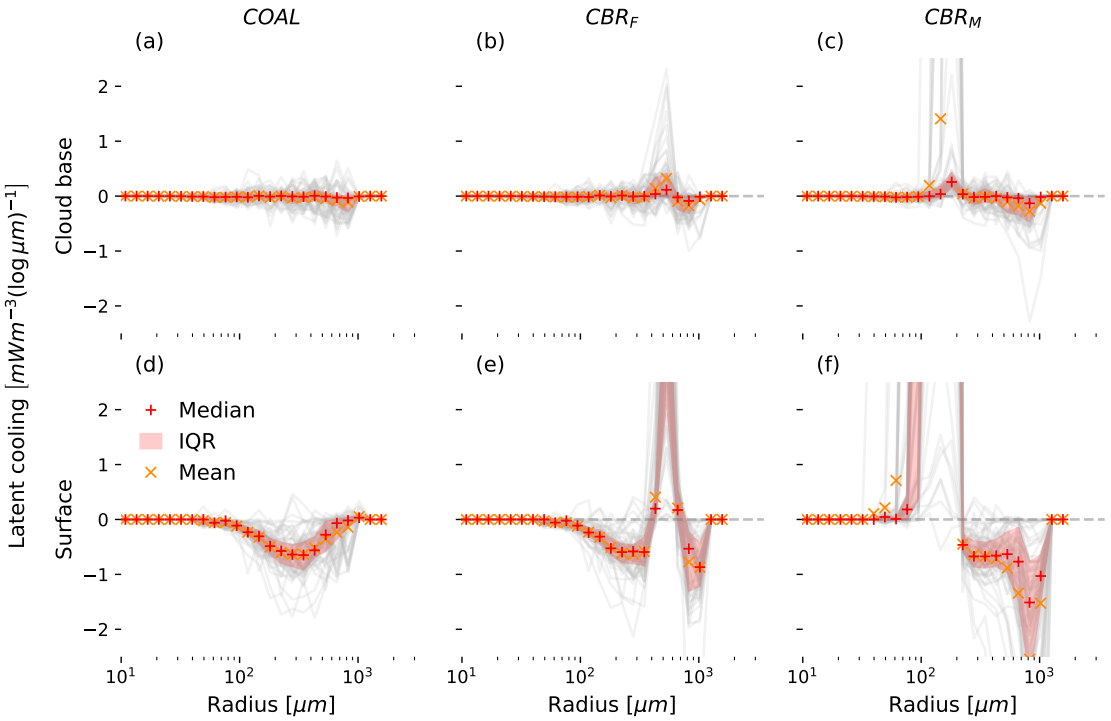

Figure 14: Difference of LC of microphysics setups to CE for equally spaced logarithmic radius bins at cloud base (a-c) and at the surface (d-f). COAL setup (a,d), CBR_F setup (b,e) and CBR_M setup (c,f). Thin grey lines are the stationary states of individual clouds. Red crossed indicate the median with red shading as the Inter Quartile Range (IQR) ($25\,\%$ to $75\,\%$ interval). Orange crosses indicate inter-cloud mean values.

radii dependency of differences between the COAL, CBR_F and CBR_M setups with the CE setup. These latent cooling differences at cloud base and at the surface are shown in Figure 14. To explain the differences, we need to consider how the individual setups transfer mass across droplet radii ranges. Figure 15 shows the difference in the MSD between the setups and the CE setup.

Near the cloud base, no pronounced difference to the CE setup can be seen for the COAL and CBR_F setups because the spread between individual clouds is prominent (Figure 14 (a,b)). Latent cooling in the COAL setup is reduced near the surface for droplets with radii between approximately $150\,\mu\mathrm{m}$ to $600\,\mu\mathrm{m}$ (Figure 14 (d)), with a peak of reduction of approximately $0.8\,\mathrm{mW\,m^{-3}}$ and thus nearly $8\,\%$ compared to the absolute latent cooling rates (Figure S13). It is a combination of this shift in the number concentration and the shift of mass (Figure 15 (d) and Figure S14 (d)). This supports our hypothesis, that the reduction in latent cooling is mainly due to the evaporation efficiency difference between the input

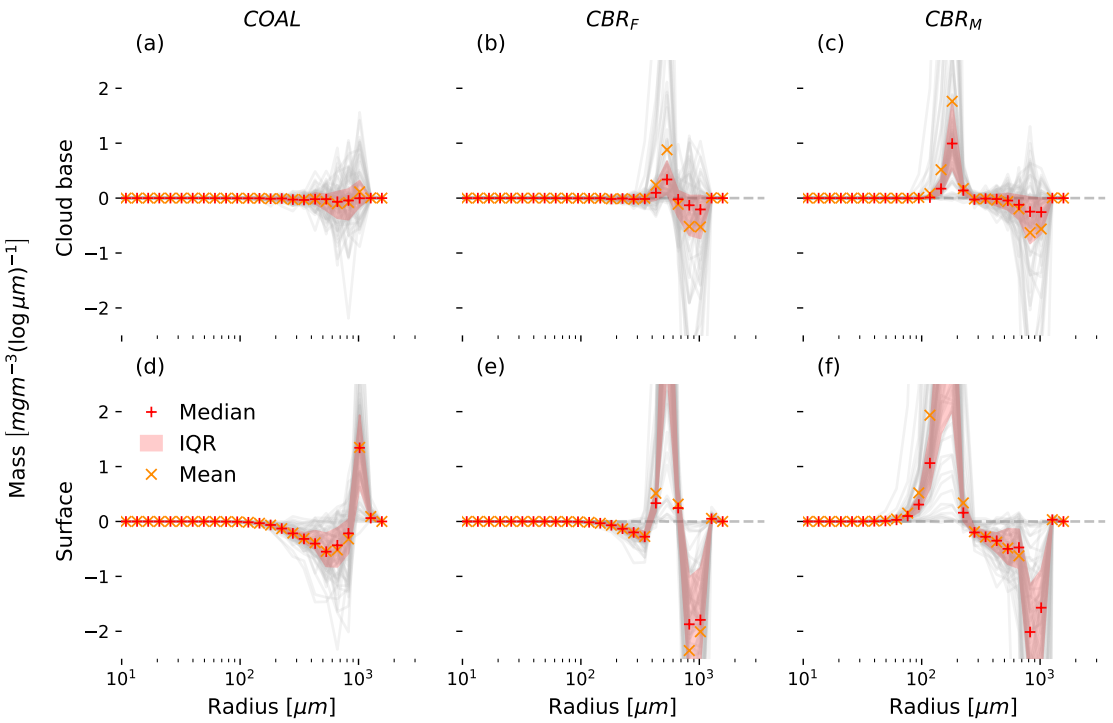

Figure 15: As Figure 14, but for the MSD or in other words the distribution of LWC.

droplets (larger) and the output droplets (smaller) for the coalescence process. The overall latent cooling reduction is linear throughout the sub cloudy layer towards the surface.

For CBR_F, the reduction in latent cooling is a superposition of the coalescence process and the breakup of a large droplet into smaller droplets. The reduction in latent cooling for droplets of radii below $250\ \mu m$ is only slightly different compared to the COAL setup, which is in line with similar differences of the mass and number concentration of droplets (Figure 15 (e) and Figure S14 (e)). There is a net shift of mass from droplets of approximately $1000\ \mu m$ radius toward droplets of approximately $500\ \mu m$ radius. The smaller droplets have one-fifth of the mass compared to the larger droplets, which is very well in line with our prescribed number of fragments of five. The overall evaporation rate is similar to the CE setup, but different droplet radii are responsible for it.

For the CBR_M setup, the peak of enhanced latent cooling is shifted towards the $100\ \mu m$ to $200\ \mu m$ range and is much stronger compared to the CBR_F setup (Figure 14 (f)). The radii range aligns with droplets being most likely to coalesce, directly counteracting the effect of coalescence. The reason is the larger prescribed number of fragments, which leads to creation of more and even smaller droplets by breakup (Figure S14 (f)). The amount of mass

which is transferred from the large droplet regime towards this smaller droplet regime is similar for CBR_F and CBR_M (Figure 15 (f,g)). But the fragments are much smaller in CBR_M than in CBR_F setup and thus evaporate the water they contain even more efficiently. Thus, the breakup with many fragments leads to much stronger latent cooling compared to all other setups.

The DSD therefore needs to be carefully prescribed. The impact of cloud properties and the thermodynamic environment rules the variability in rain evaporation during EUREC^{4}A. We find the microphysics to lead to systematic differences of less than $10\,\%$ for all clouds, which are neglectable compared to the inter-cloud spread. For the three more realistic setups, we find only a small impact of the microphysics on the overall evaporation and latent cooling in the sub cloud layer. We postulate the qualitative relation will remain the same when adjusting the LWC because the shape of the DSD should remain the same. Changing the shape of the distribution on the other hand could have strong impacts on rain evaporation and latent cooling.

4 Conclusion and Outlook

The evaporation of rain below the cloud base is a crucial process and affects surface precipitation and the energy balance of the sub cloud layer of shallow convective trade cumulus clouds. As an important driver for cold pools, it can alter the total cloud cover and mesoscale organization of trade cumulus clouds (Vogel et al., 2021). In this study, we demonstrate a novel approach to estimate rain evaporation and corresponding latent cooling with a 1D rainshaft implementation of the newly developed Super-Droplet-Model CLEO by Bayley et al., n.d. We estimate evaporation over a wide range of initial droplet size distribution (DSD) and thermodynamic profiles, based on measurements from the EUREC^{4}A campaign of 111 identified clouds (Bony et al., 2022; Coutris, 2021; George, 2021; George et al., 2021; Stevens et al., 2021). There is a wide discussion about cloud identification, and even instruments from the same aircraft show discrepancies (Konow et al., 2021). Nevertheless, we use individual clouds to understand the importance of the inter-cloud differences, making our approach different from Sarkar et al., 2023, who analysed individual flight lags lasting multiple hours.

By reaching a stationary state in our simulations, we model a snapshot of the sub cloud layer beneath the identified clouds. We find an inter-cloud mean column integrated latent cooling (LC_{CI}) of $32.7 \pm 1.0\,\mathrm{W\,m^{-2}}$ for our condensation only setup (CE) and an inter-cloud spread of $12\,\mathrm{W\,m^{-2}}$ to $58\,\mathrm{W\,m^{-2}}$. Our evaporation rates and latent cooling (LC) are considerably lower than the findings by Sarkar et al., 2023. We also find lower values compared to the radar retrieved evaporation taken from deeper continental convection by Tridon et al., 2017.

The LWC at cloud base is a dominant driver in determining the strength of LC_{CI} in the sub cloud layer by explaining approximately $50\,\%$ of the inter-cloud variability ($R = 0.71$). Further, due to an underestimation of the cloud base liquid water content (LWC) in our initial conditions, our estimates for precipitation intensity are lower than the climatological values found by Vogel et al., 2021. We plan to increasing cloud base LWC by a better fit of the DSD, which should lead to higher evaporation rates. But also, our estimated rain evaporated

fraction of $7.1 \pm 0.9\,\%$ is significantly lower than the estimates given by Sarkar et al., 2023, for similar ranges of cloud base LWC. They also identified more top-heavy profiles, whereas we find more bottom-heavy LC profiles. Both differences might be due to our initial DSDs containing more large ($1\,\mathrm{mm}$) and less small droplets ($100\,\mu\mathrm{m}$) than those used by Sarkar et al., 2023. Distributing the same amount of water across a few large droplets rather than many small ones, results in a smaller surface area, leading to less evaporation in a given time. The evaporation efficiency is lower. Large droplets also fall deeper into the sub cloud layer, leading to more bottom-heavy profiles. A detailed analysis is still necessary.

By prescribing a variety of relative humidity profiles, we show that stronger gradients in relative humidity lead to larger LC near the surface compared to the cloud base. The slope of the relative humidity profiles explains approximately $67\,\%$ of the inter-cloud variability of the latent cooling vertical gradient ($R = -0.82$). But our prescribed relative humidity profiles do not show saturation near cloud base. Therefore, we will fit the cloud base relative humidity to be approximately $100\,\%$ in the future.

The novel use of the Super-Droplet-Model CLEO allows us to incorporate collision coalescence, breakup and rebound due to droplet-droplet interaction in four microphysical setups. For the Coalescence setup (COAL), we can identify a reduction in LC of approximately $10\,\%$ near the surface, due to this shift in the MSD. We find breakup to counteract this reduction in LC, by distributing water in large droplets to many small droplets, increasing evaporation efficiency. The enhancement of evaporation due to breakup depends strongly on the number of fragments produced within each breakup process. With a very high number of fragments (125), the LC is enhanced by a factor of four compared to the CE setup. We find the microphysics to lead to systematic differences for all clouds, but being much weaker than the inter-cloud spread. In summary, we find the impact of cloud properties and the thermodynamic environment to rule the variability in rain evaporation during EUREC^{4}A. Therefore, we are confident, that methods excluding droplet-droplet interactions can still yield good estimates of rain evaporation.

To better understand the uncertainty of our method, sensitivity experiments on our setup would be of great interest. Especially the impact of the number of super-droplets is crucial to guide the model developers to a correct representation of rain evaporation with as little computational effort as possible, by using the lowest number of super-droplets necessary for realistic simulations. To better disentangle the effects of the cloud base DSD and the humidity profiles, idealized sensitivity test are planned.

More detailed comparisons to the results of other schemes and setups (Sarkar et al., 2023;

Seifert, 2008; Wood, 2005) with identical initial conditions will help to clearly identify inter-scheme differences. Direct comparison to the radar-retrieved DSDs by Tridon et al., 2017 will help to understand how well our method simulates the sub cloud layer DSD. Using the radar retrieval method from Tridon et al., 2017, we plan to compute retrievals of the cloud base DSD from long term measurements of the Barbados Cloud Observatory and the data from ORCESTRAs sub-campaign SCORE. Additionally, direct applications of our method on DSD measurements taken onboard of the ATR aircraft during ORCESTRAs sub-campaign MAESTRO are planned [1].
With our setup, we also build a bridge to future ICON simulations with CLEO by assessing the performance of CLEO in our setup.

As a long term goal, we wish to give an overreaching number for the total rain evaporation and its uncertainty over the northern Atlantic trade wind region, to close our knowledge gap on the sub cloud layer energetics.

[1] With the ORCESTRA campaign, knowledge gaps shall be closed in the understanding of how physical mechanisms organize tropical convection at the mesoscale. It takes place in August and September 2024 in the tropical Atlantic. SCORE is one of ORCESTRAs sub-campaigns and specifically aims to better understand sub cloud layer rain evaporation using observations from the Barbados Cloud Observatory.

5 References

Bao, J., & Windmiller, J. M. (2021). Impact of microphysics on tropical precipitation extremes in a global storm-resolving model. *Geophysical Research Letters*, *48*(13), e2021GL094206. https://doi.org/10.1029/2021GL094206

Bayley, C. (2024a). *CLEO 0.1.0 documentation*. Retrieved August 23, 2024, from https://yoctoyotta1024.github.io/CLEO/

Bayley, C. (2024b). *Yoctoyotta1024/CLEO* (Version v0.21.0). Max-Planck-Institut für Meteorologie. Retrieved September 4, 2024, from https://github.com/yoctoyotta1024/CLEO

Bayley, C., Kölling, D. T., Naumann, D. A. K., Vogel, R., Shima, S.-I., & Stevens, B. (n.d.). CLEO: A super-droplet model with a high 2 performance computational implementation and 3 droplet breakup algorithm.

Bony, S., & Dufresne, J.-L. (2005). Marine boundary layer clouds at the heart of tropical cloud feedback uncertainties in climate models. *Geophysical Research Letters*, *32*(20). https://doi.org/10.1029/2005GL023851

Bony, S., Lothon, M., Delanoë, J., Coutris, P., Etienne, J.-C., Aemisegger, F., Albright, A. L., André, T., Bellec, H., Baron, A., Bourdinot, J.-F., Brilouet, P.-E., Bourdon, A., Canonici, J.-C., Caudoux, C., Chazette, P., Cluzeau, M., Cornet, C., Desbios, J.-P., … Vogel, R. (2022). EUREC^{4}a observations from the SAFIRE ATR42 aircraft. *Earth System Science Data*, *14*(4), 2021–2064. https://doi.org/10.5194/essd-14-2021-2022

Bony, S., Schulz, H., Vial, J., & Stevens, B. (2020). Sugar, gravel, fish, and flowers: Dependence of mesoscale patterns of trade-wind clouds on environmental conditions. *Geophysical Research Letters*, *47*(7), e2019GL085988. https://doi.org/10.1029/2019GL085988

Bony, S., Stevens, B., Frierson, D. M. W., Jakob, C., Kageyama, M., Pincus, R., Shepherd, T. G., Sherwood, S. C., Siebesma, A. P., Sobel, A. H., Watanabe, M., & Webb, M. J. (2015). Clouds, circulation and climate sensitivity. *Nature Geoscience*, *8*(4), 261–268. https://doi.org/10.1038/ngeo2398

Coutris, P. (2021). SAFIRE ATR42: PMA/cloud composite dataset. https://doi.org/10.25326/237

Feingold, G., & Levin, Z. (1986). The lognormal fit to raindrop spectra from frontal convective clouds in israel. *Journal of Applied Meteorology and Climatology*, *25*(10), 1346–1363. https://doi.org/10.1175/1520-0450(1986)025<1346:TLFTRS>2.0.CO;2

George, G. (2021). JOANNE-dataset: Joint dropsonde observations of the atmosphere in tropical north atlaNtic meso-scale environments (v2.0.0). https://doi.org/10.25326/246

George, G., Stevens, B., Bony, S., Pincus, R., Fairall, C., Schulz, H., Kölling, T., Kalen, Q. T., Klingebiel, M., Konow, H., Lundry, A., Prange, M., & Radtke, J. (2021). JOANNE: Joint dropsonde observations of the atmosphere in tropical north atlaNtic meso-scale environments. *Earth System Science Data*, *13*(11), 5253–5272. https://doi.org/10.5194/essd-13-5253-2021

Grabowski, W. W., Dziekan, P., & Pawlowska, H. (2018). Lagrangian condensation microphysics with twomey CCN activation. *Geoscientific Model Development*, *11*(1), 103–120. https://doi.org/10.5194/gmd-11-103-2018

Gunn, R., & Kinzer, G. D. (1949). THE TERMINAL VELOCITY OF FALL FOR WATER DROPLETS IN STAGNANT AIR. *Journal of Meteorology*, *6*(4), 243–248. https://doi.org/10.1175/1520-0469(1949)006<0243:TTVOFF>2.0.CO;2

Hu, Z., & Srivastava, R. C. (1995). Evolution of raindrop size distribution by coalescence, breakup, and evaporation: Theory and observations. *Journal of the Atmospheric Sciences*, *52*(10), 1761–1783. https://doi.org/10.1175/1520-0469(1995)052<1761:EORSDB>2.0.CO;2

Köhler, H. (1936). The nucleus in and the growth of hygroscopic droplets. *Transactions of the Faraday Society*, *32*(0), 1152–1161. https://doi.org/10.1039/TF9363201152

Konow, H., Ewald, F., George, G., Jacob, M., Klingebiel, M., Kölling, T., Luebke, A. E., Mieslinger, T., Pörtge, V., Radtke, J., Schäfer, M., Schulz, H., Vogel, R., Wirth, M., Bony, S., Crewell, S., Ehrlich, A., Forster, L., Giez, A., … Stevens, B. (2021). EUREC^{4}a's *HALO*. *Earth System Science Data*, *13*(12), 5545–5563. https://doi.org/10.5194/essd-13-5545-2021

Leandro, M., & Chuang, P. (2021). ATOMIC aircraft microphysics: Size-resolved cloud and aerosol number concentrations taken from n43 aircraft in the north atlantic ocean, barbados: Atlantic tradewind ocean-atmosphere mesoscale interaction campaign 2020-01-31 to 2020-02-10 (NCEI accession 0232458). https://doi.org/10.25921/VWVQ-5015

Li, Z., Zuidema, P., & Zhu, P. (2014). Simulated convective invigoration processes at trade wind cumulus cold pool boundaries. *Journal of the Atmospheric Sciences*, *71*(8), 2823–2841. https://doi.org/10.1175/JAS-D-13-0184.1

Lohmann, U., Lüönd, F., & Mahrt, F. (2016, April 30). *An introduction to clouds: From the microscale to climate* (1st ed.). Cambridge University Press. https://doi.org/10.1017/CBO9781139087513

Long, A. B. (1974). Solutions to the droplet collection equation for polynomial kernels. *Journal of the Atmospheric Sciences*, *31*(4), 1040–1052. https://doi.org/10.1175/1520-0469(1974)031<1040:STTDCE>2.0.CO;2

Marshall, J. S., & Palmer, W. M. K. (1948). THE DISTRIBUTION OF RAINDROPS WITH SIZE. *Journal of the Atmospheric Sciences*, *5*(4), 165–166. https://doi.org/10.1175/1520-0469(1948)005<0165:TDORWS>2.0.CO;2

Morrison, H., van Lier-Walqui, M., Fridlind, A. M., Grabowski, W. W., Harrington, J. Y., Hoose, C., Korolev, A., Kumjian, M. R., Milbrandt, J. A., Pawlowska, H., Posselt, D. J., Prat, O. P., Reimel, K. J., Shima, S.-I., van Diedenhoven, B., & Xue, L. (2020). Confronting the challenge of modeling cloud and precipitation microphysics. *Journal of Advances in Modeling Earth Systems*, *12*(8), e2019MS001689. https://doi.org/10.1029/2019MS001689

Naumann, A. K., & Seifert, A. (2016). Evolution of the shape of the raindrop size distribution in simulated shallow cumulus. *Journal of the Atmospheric Sciences*, *73*(6), 2279–2297. https://doi.org/10.1175/JAS-D-15-0263.1

Nuijens, L., Serikov, I., Hirsch, L., Lonitz, K., & Stevens, B. (2014). The distribution and variability of low-level cloud in the north atlantic trades. *Quarterly Journal of the Royal Meteorological Society*, *140*(684), 2364–2374. https://doi.org/10.1002/qj.2307

Nuijens, L., Stevens, B., & Siebesma, A. P. (2009). The environment of precipitating shallow cumulus convection. *Journal of the Atmospheric Sciences*, *66*(7), 1962–1979. https://doi.org/10.1175/2008JAS2841.1

Pincus, R., Fairall, C. W., Bailey, A., Chen, H., Chuang, P. Y., de Boer, G., Feingold, G., Henze, D., Kalen, Q. T., Kazil, J., Leandro, M., Lundry, A., Moran, K., Naeher, D. A., Noone, D., Patel, A. J., Pezoa, S., PopStefanija, I., Thompson, E. J., … Zuidema, P. (2021). Observations from the NOAA p-3 aircraft during ATOMIC. *Earth System Science Data*, *13*(7), 3281–3296. https://doi.org/10.5194/essd-13-3281-2021

Rogers, R. R., Baumgardner, D., Ethier, S. A., Carter, D. A., & Ecklund, W. L. (1993). Comparison of raindrop size distributions measured by radar wind profiler and by airplane. *Journal of Applied Meteorology and Climatology*, *32*(4), 694–699. https://doi.org/10.1175/1520-0450(1993)032<0694:CORSDM>2.0.CO;2

Rogers, R., & Yau, M. (1989). *A short course in cloud physics - 3rd edition*. Elsevier. Retrieved October 27, 2023, from https://shop.elsevier.com/books/a-short-course-in-cloud-physics/yau/978-0-08-057094-5

Sarkar, M., Bailey, A., Blossey, P., De Szoeke, S. P., Noone, D., Quiñones Meléndez, E., Leandro, M. D., & Chuang, P. Y. (2023). Sub-cloud rain evaporation in the north atlantic winter trade winds derived by pairing isotopic data with a bin-resolved microphysical model. *Atmospheric Chemistry and Physics*, *23*(19), 12671–12690. https://doi.org/10.5194/acp-23-12671-2023

Seifert, A. (2008). On the parameterization of evaporation of raindrops as simulated by a one-dimensional rainshaft model. *Journal of the Atmospheric Sciences*, *65*(11), 3608–3619. https://doi.org/10.1175/2008JAS2586.1

Seifert, A., & Beheng, K. D. (2001). A double-moment parameterization for simulating autoconversion, accretion and selfcollection. *Atmospheric Research*, *59-60*, 265–281. https://doi.org/10.1016/S0169-8095(01)00126-0

Shima, S., Kusano, K., Kawano, A., Sugiyama, T., & Kawahara, S. (2009). The super-droplet method for the numerical simulation of clouds and precipitation: A particle-based and probabilistic microphysics model coupled with a non-hydrostatic model: SUPER-DROPLET METHOD FOR CLOUDS AND PRECIPITATION. *Quarterly Journal of the Royal Meteorological Society*, *135*(642), 1307–1320. https://doi.org/10.1002/qj.441

Simmel, M., Trautmann, T., & Tetzlaff, G. (2002). Numerical solution of the stochastic collection equation—comparison of the linear discrete method with other methods. *Atmospheric Research*, *61*(2), 135–148. https://doi.org/10.1016/S0169-8095(01)00131-4

Stevens, B. (2005). ATMOSPHERIC MOIST CONVECTION. *Annual Review of Earth and Planetary Sciences*, *33*, 605–643. https://doi.org/10.1146/annurev.earth.33.092203.122658

Stevens, B., Bony, S., Farrell, D., Ament, F., Blyth, A., Fairall, C., Karstensen, J., Quinn, P. K., Speich, S., Acquistapace, C., Aemisegger, F., Albright, A. L., Bellenger, H., Bodenschatz, E., Caesar, K.-A., Chewitt-Lucas, R., de Boer, G., Delanoë, J., Denby, L., … Zöger, M. (2021). EUREC^{4}a. *Earth System Science Data*, *13*(8), 4067–4119. https://doi.org/10.5194/essd-13-4067-2021

Straub, W., Beheng, K. D., Seifert, A., Schlottke, J., & Weigand, B. (2010). Numerical investigation of collision-induced breakup of raindrops. part II: Parameterizations of coalescence efficiencies and fragment size distributions. *Journal of the Atmospheric Sciences*, *67*(3), 576–588. https://doi.org/10.1175/2009JAS3175.1

Touzé-Peiffer, L., Vogel, R., & Rochetin, N. (2022). Cold pools observed during EUREC4a: Detection and characterization from atmospheric soundings. *Journal of Applied Meteorology and Climatology*, *61*(5), 593–610. https://doi.org/10.1175/JAMC-D-21-0048.1

Tridon, F., Battaglia, A., & Watters, D. (2017). Evaporation in action sensed by multiwavelength doppler radars. *Journal of Geophysical Research: Atmospheres*, *122*(17), 9379–9390. https://doi.org/10.1002/2016JD025998

Ulbrich, C. W. (1983). Natural variations in the analytical form of the raindrop size distribution. *Journal of Applied Meteorology and Climatology*, *22*(10), 1764–1775. https://doi.org/10.1175/1520-0450(1983)022<1764:NVITAF>2.0.CO;2

vanZanten, M. C., Stevens, B., Nuijens, L., Siebesma, A. P., Ackerman, A. S., Burnet, F., Cheng, A., Couvreux, F., Jiang, H., Khairoutdinov, M., Kogan, Y., Lewellen, D. C., Mechem, D., Nakamura, K., Noda, A., Shipway, B. J., Slawinska, J., Wang, S., & Wyszogrodzki, A. (2011). Controls on precipitation and cloudiness in simulations of trade-wind cumulus as observed during RICO. *Journal of Advances in Modeling Earth Systems*, *3*(2). https://doi.org/10.1029/2011MS000056

Vial, J., Bony, S., Stevens, B., & Vogel, R. (2017). Mechanisms and model diversity of trade-wind shallow cumulus cloud feedbacks: A review. *Surveys in Geophysics*, *38*(6), 1331–1353. https://doi.org/10.1007/s10712-017-9418-2

Vogel, R., Konow, H., Schulz, H., & Zuidema, P. (2021). A climatology of trade-wind cumulus cold pools and their link to mesoscale cloud organization. *Atmospheric Chemistry and Physics*, *21*(21), 16609–16630. https://doi.org/10.5194/acp-21-16609-2021

Wood, R. (2005). Drizzle in stratiform boundary layer clouds. part II: Microphysical aspects. *Journal of the Atmospheric Sciences*, *62*(9), 3034–3050. https://doi.org/10.1175/JAS3530.1

Glossary and Abbreviations

LC Latent cooling by evaporation. 15, 19–23, 25, 26, 28, 31, 32, 49, 50

LC_{CI} Column integrated latent cooling. 19–21, 31, 49, 50

CBR$_F$ Model setup containing condensation and evaporation and collision coalescence, breakup and rebound with a fixed number of framents ($n = 5$). 11, 26–30, 52

CBR$_M$ Model setup containing condensation and evaporation and collision coalescence, breakup and rebound with a fixed number of framents ($n = 125$). 11, 25–30, 52

CE Model setup containing condensation and evaporation. 11, 17, 19, 23, 24, 26–29, 31, 32, 47, 52

CLEO Super-Droplet-Model created by Clara Bayley. 3, 10, 13, 15, 31–33, I

cloud composite Dataset from the SAFIRE ATR42 airplane with DSD measurment along flight track. 5, 6, 43

COAL Model setup containing condensation and evaporation and collision coalescence. 11, 26–29, 32, 52

DSD Droplet size distribution. 1–8, 11–13, 18–20, 22, 23, 25, 26, 30–33, 41, 44

LWC Liquid water content. 2, 13, 14, 18–24, 29–32, 47–49

MSD Mass size distribution. 23–26, 28, 29, 32

super-droplet A Super-Droplet represents a certain number of real droplets with similar attributes (e.g. radius). 3, 12–18, 32, 45, 46

Supplementary Material

Data Availability

Code for this study can be found in the two GitHub repositories nilsnevertree/CLEO-sdm-eurec4a and nilsnevertree/sdm-eurec4a.

Supplementary Figures

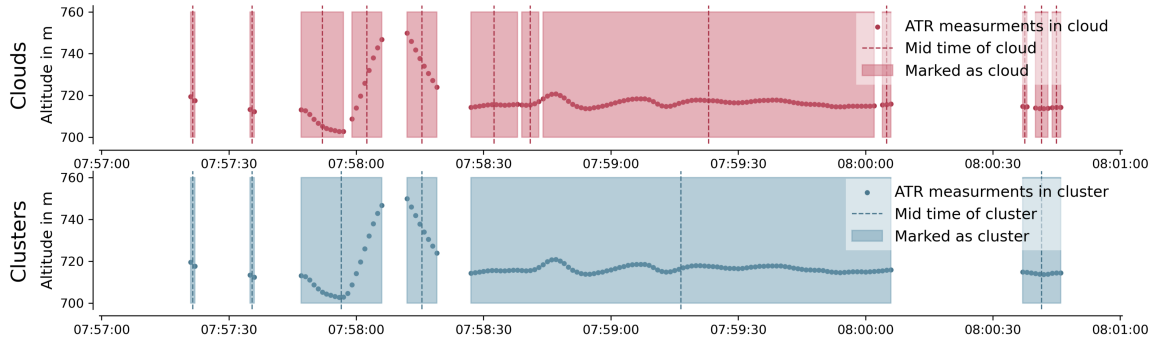

Figure S1: Bottom and top both show the flight altitude for the ATR aircraft against time from the cloud composite dataset from the 2024-02-11 at local time. Only measurements with a `True` value for the rain mask are shown in the top. In the bottom, our relaxed criterion allows individual clouds which are closely measured to be considered as a single cloud (here referred to as cloud clusters). Relaxation criterion is that $5\,\mathrm{s}$ allowed to be in-between `True` value for the rain mask. The shading indicates the duration of an individual cloud or cloud cluster. The first two cloud clusters only consist of two measurements and are not simulated.

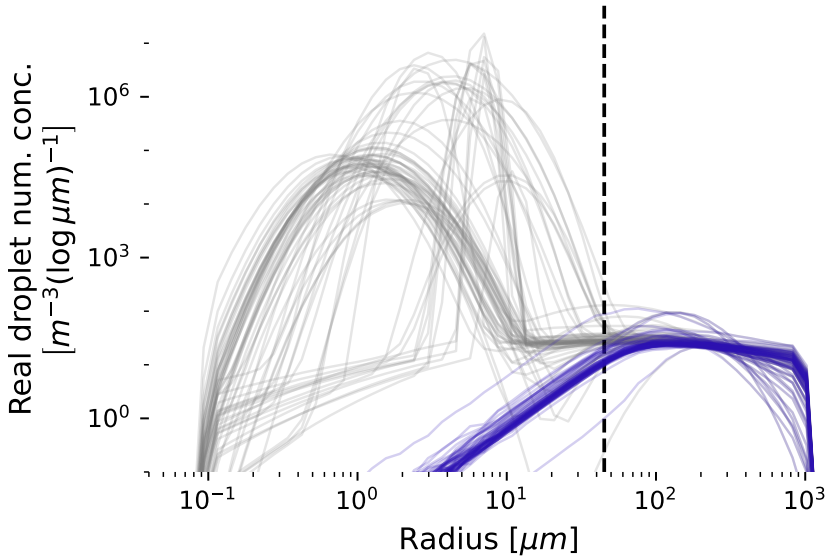

Figure S2: For each cloud, shown are the model initialisation DSD in grey and the cloud base DSD in dark blue.

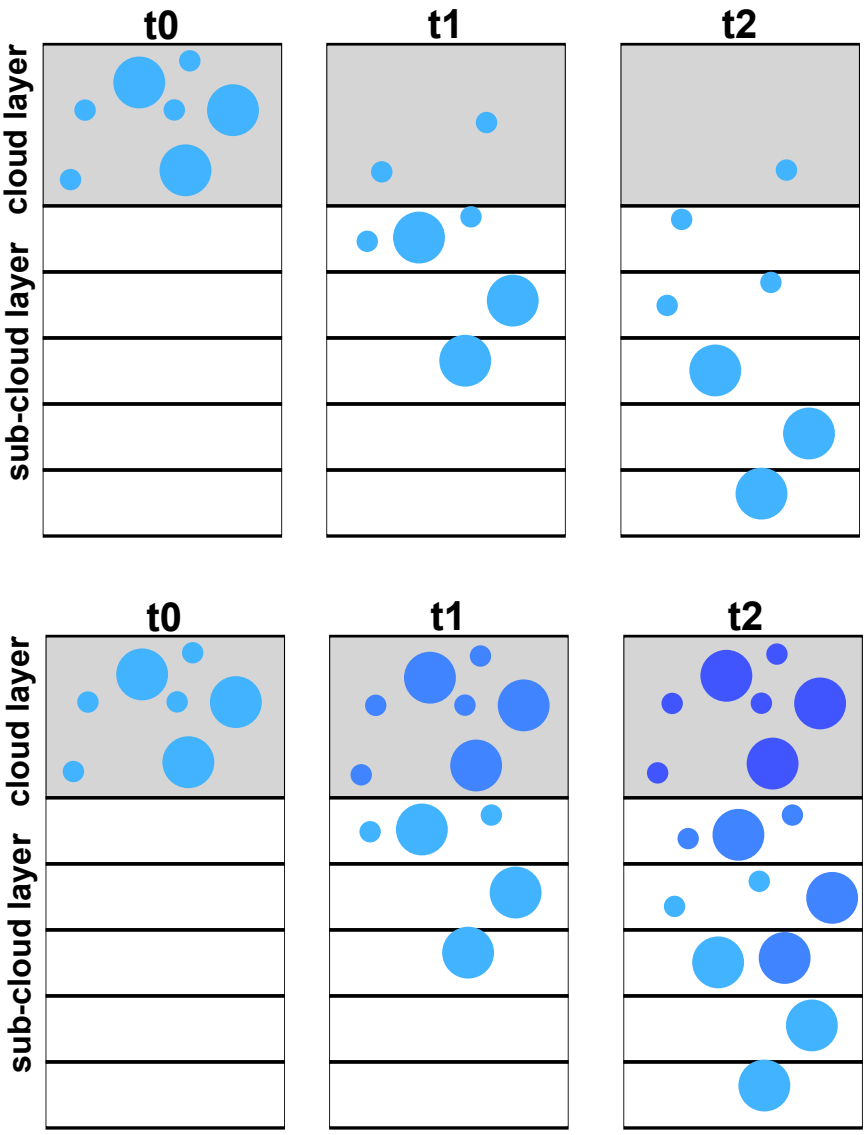

Figure S3: Bottom, as Figure 4. Top for an initialisation ofsuper-droplets only at the beginning of the simulation. Gravitational sorting leads to droplet-droplet interaction over radii ranges in the lower gridboxes.

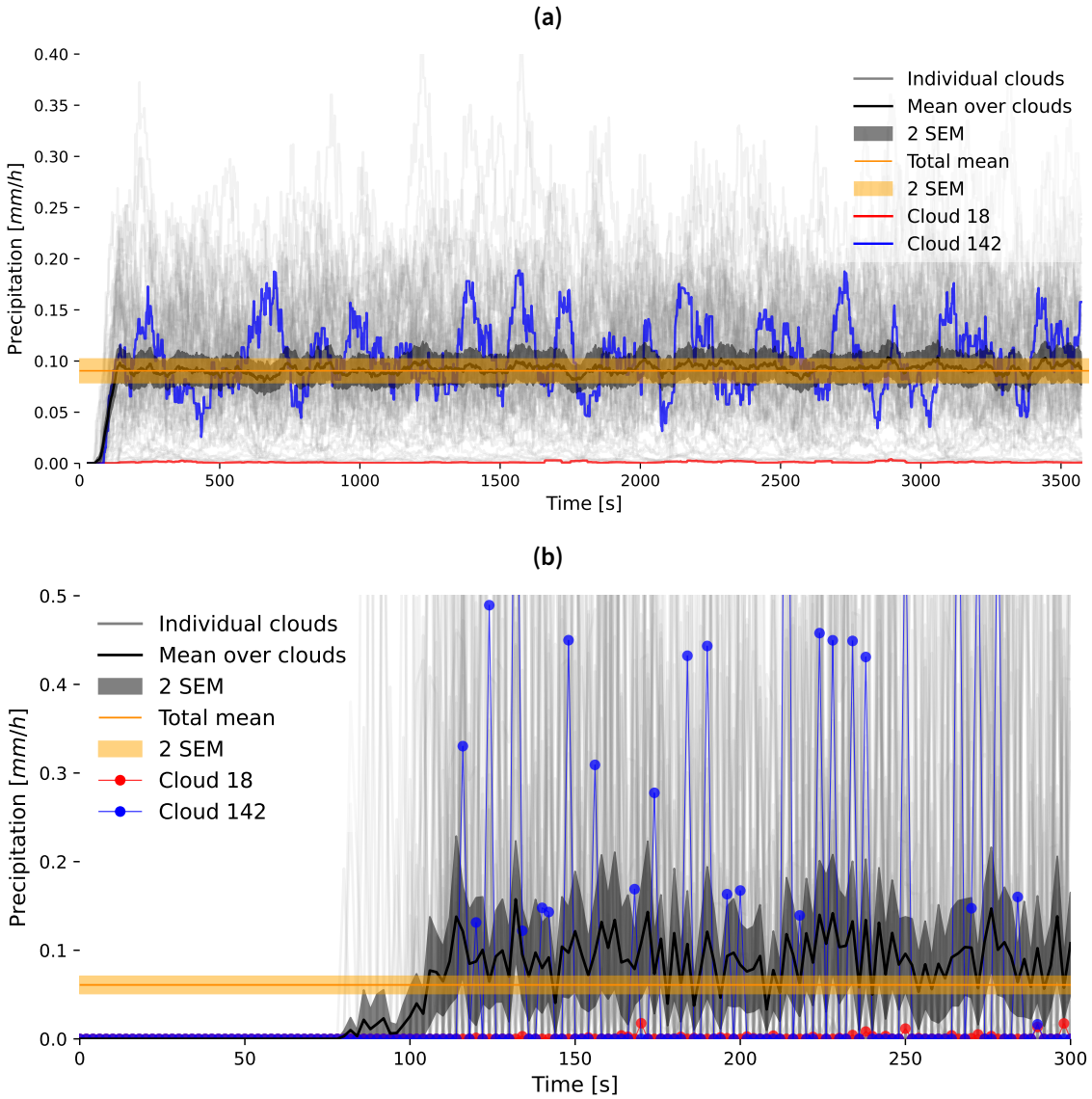

Figure S4: (a) as Figure 5 but highlighted are two individual clouds in red and blue. (b) shows the same results, but only for the first $300\,\mathrm{s}$ and without smoothing by a rolling mean. Events of individual super-droplets precipitating out of the domain can be seen as spikes and marked as red and blue dots for both selected clouds.

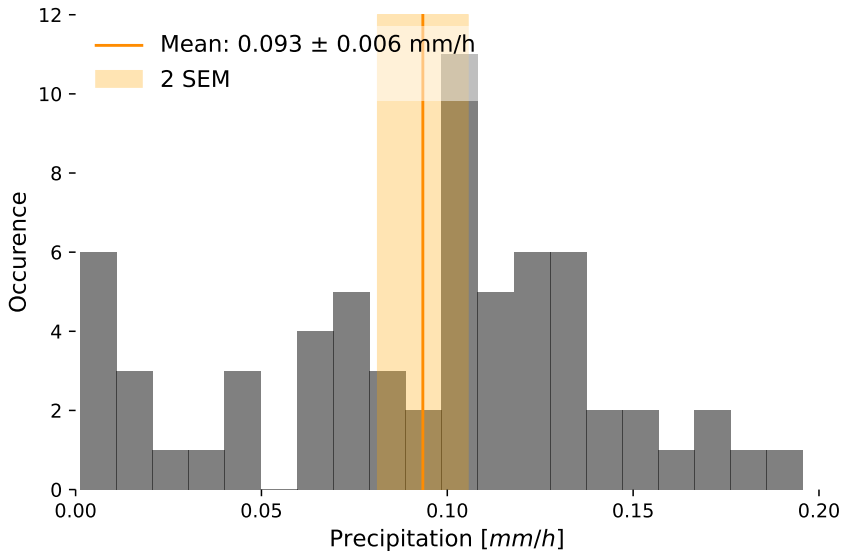

Figure S5: Distribution of all temporal mean precipitation rates for all clouds $\overline{P}^{(t)}$. Orange vertical line as mean over all clouds ($\overline{P}^{(t,c)}$) and double SEM as orange shading.

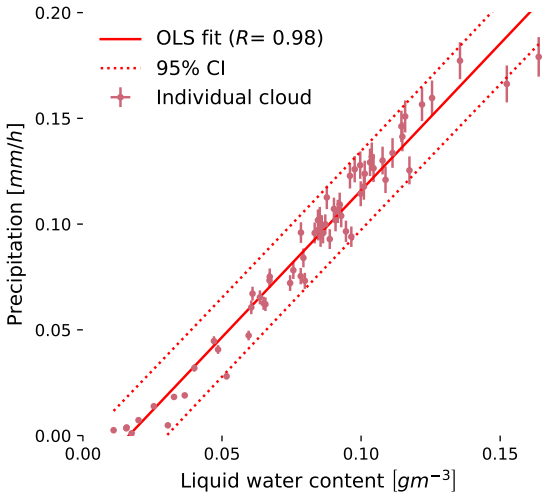

Figure S6: The precipitation and the LWC for each cloud of the CE simulations. The linear regression for them and the confidence intervals are shown in red solid and red dashed lines. Pearson correlation coefficient in legend.

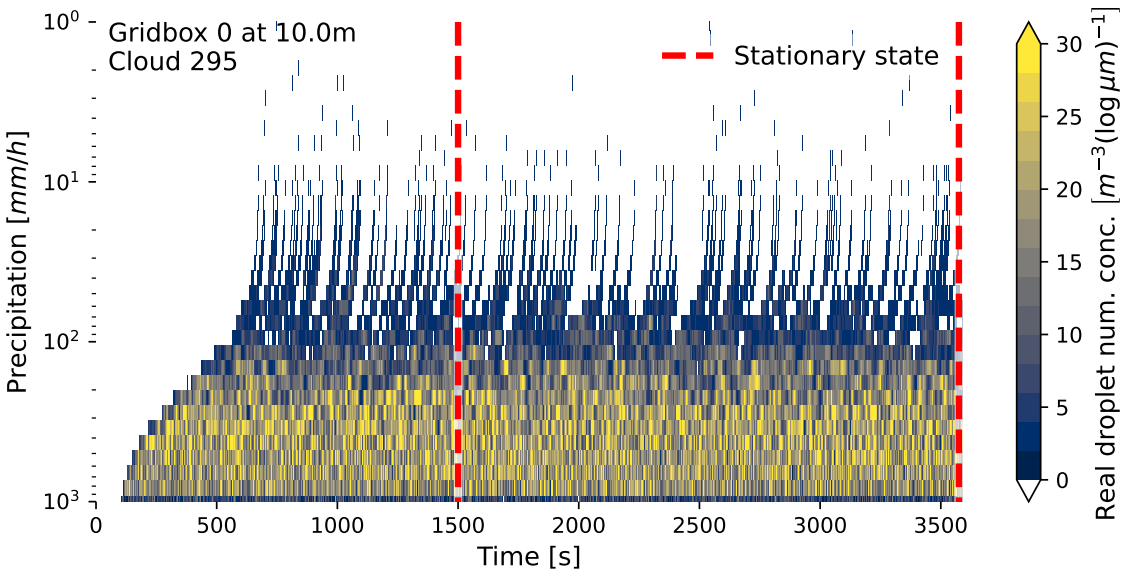

Figure S7: Temporal evolution of the real droplet number concentration per radius bin for the lowest gridbox (surface) for randomly chosen cloud (ID 295). Radius bins are equally spaced and logarithmic scaled. Red vertical dashed lines as in Figure 5.

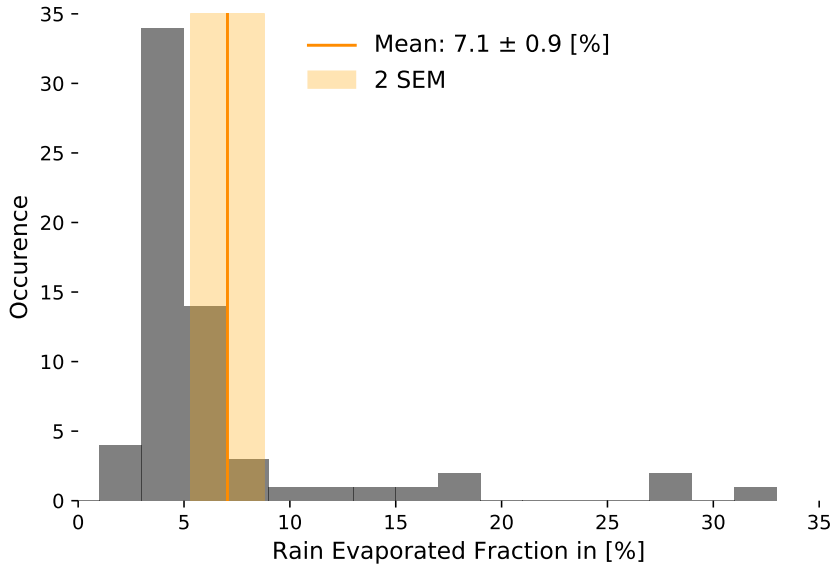

Figure S8: Histogram of the rain evaporated fraction for each cloud. Rain evaporated fraction is the difference of cloud base and surface LWC.

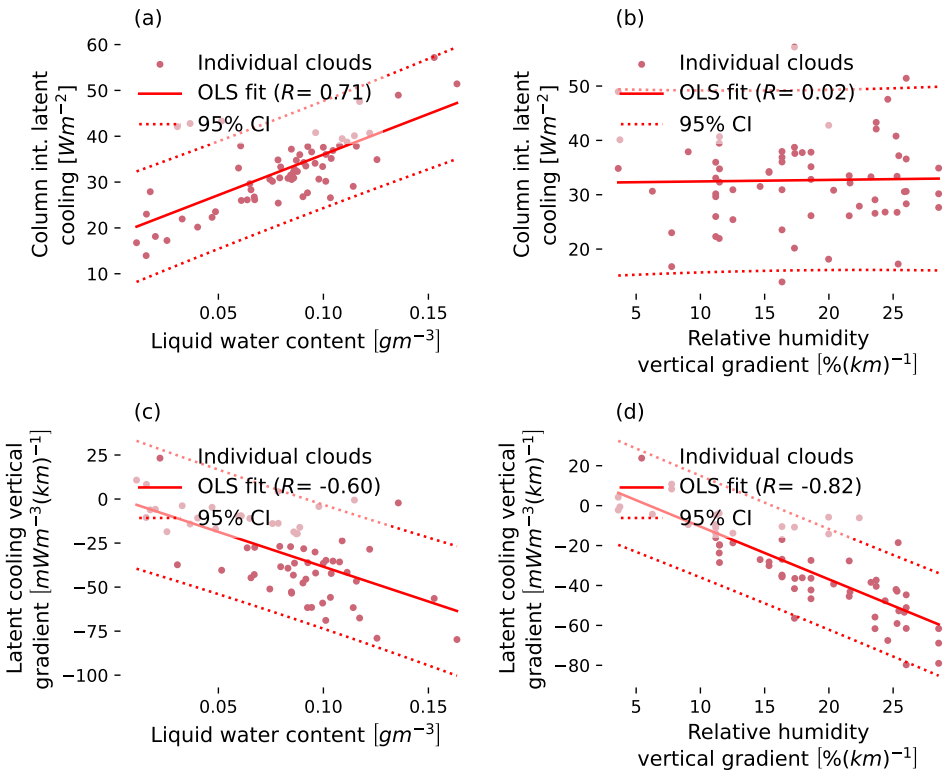

Figure S9: As Figure 9, but also shows regression of LC_{CI} against vertical gradient of relative humidity (b) and vertical gradient of LC against LWC (c).

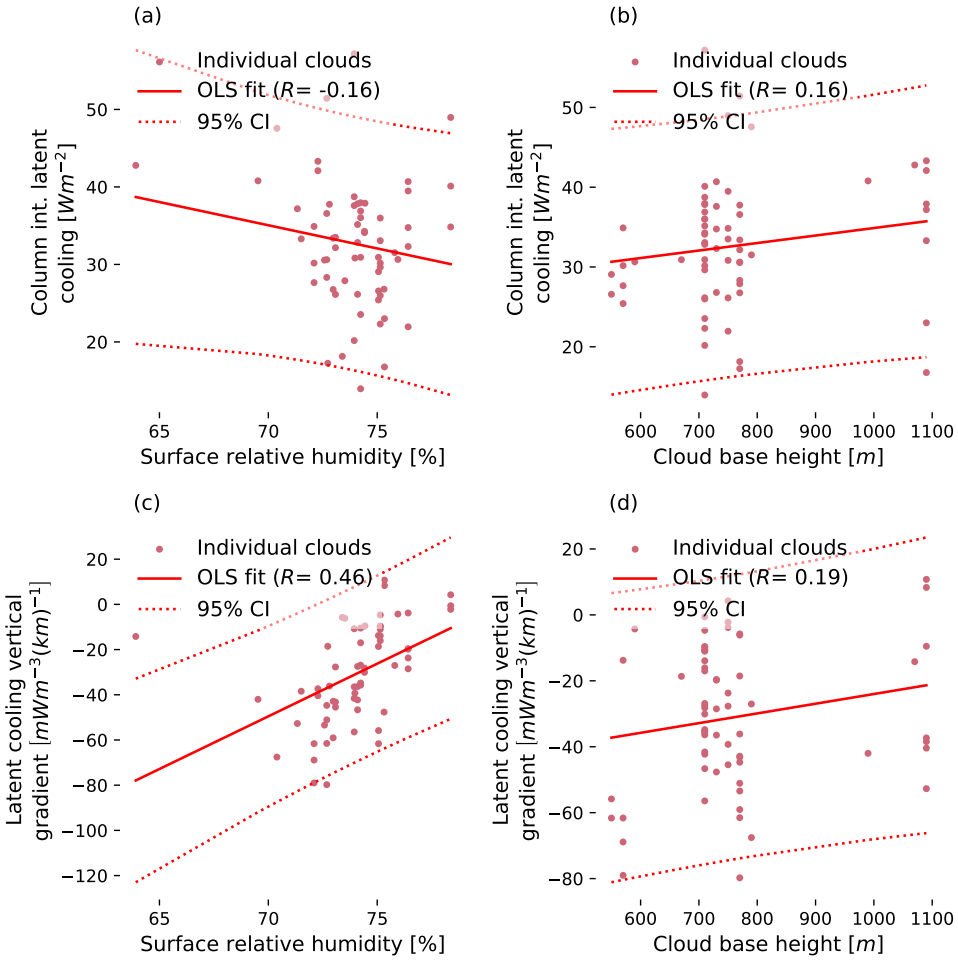

Figure S10: As Figure 9 and Figure S9, but for regression between the pairs of surface relative humidity & cloud base height and LC_{CI} & vertical gradient of LC.

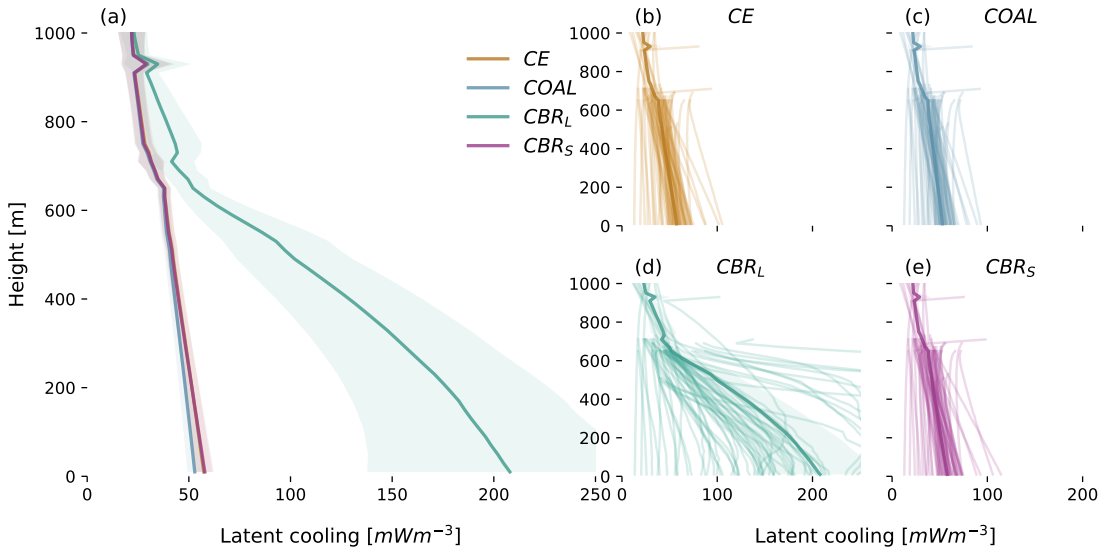

Figure S11: As Figure 12, but for all clouds simulated in this study with a wider latent cooling scale. The mean is still calculated over each gridbox. No normalization of the cloud base height is performed.

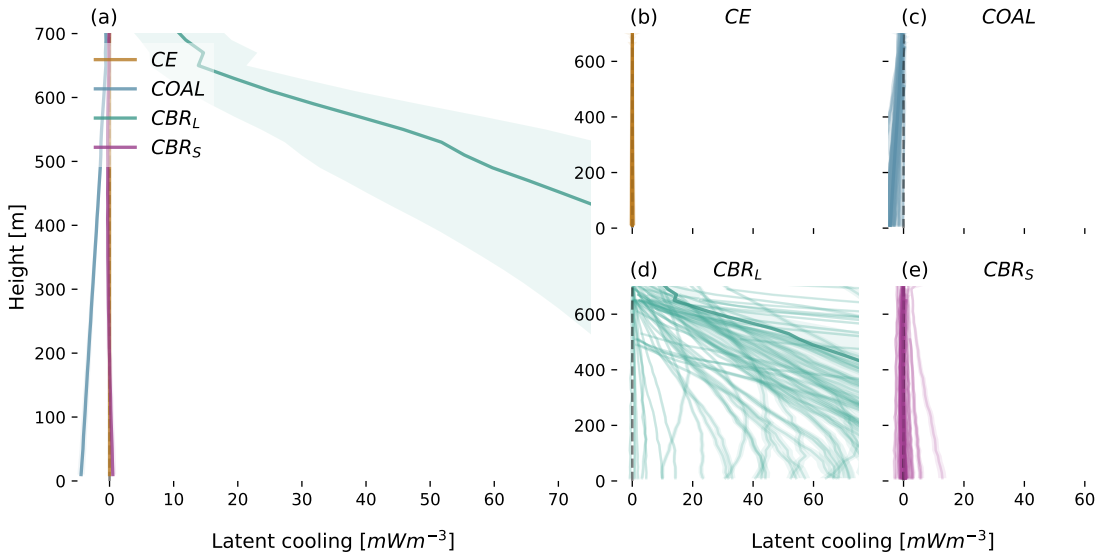

Figure S12: As Figure 13, but for all clouds simulated in this study with a wider latent cooling scale. The mean is still calculated over each gridbox. No normalization of the cloud base height is performed.

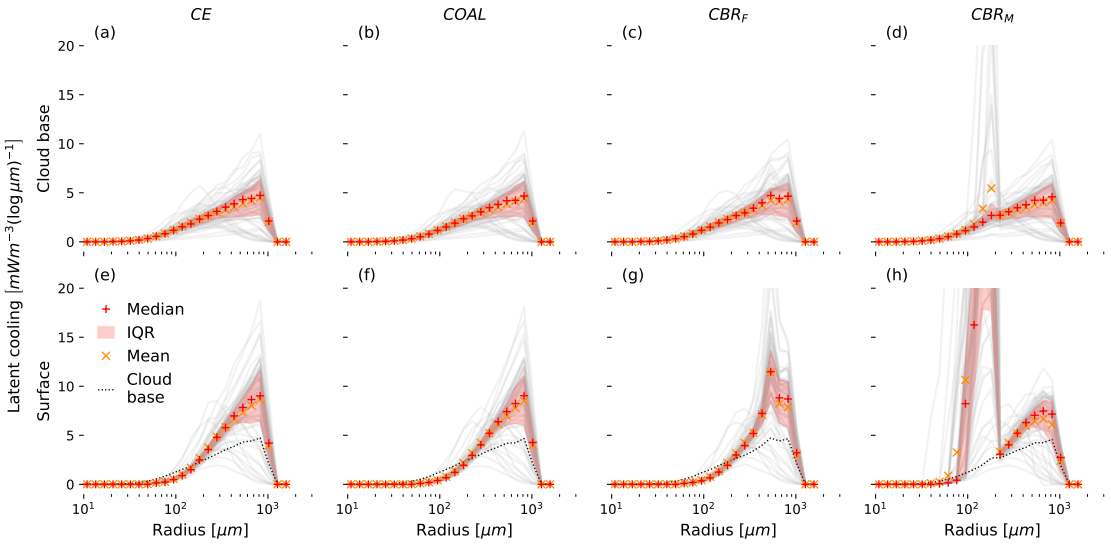

Figure S13: Similar to Figure 14, but shown is the total latent cooling dependent on radii for all setups, CE (a,e), COAL (b,f), CBR_F (c,g) and CBR_M (d,h).

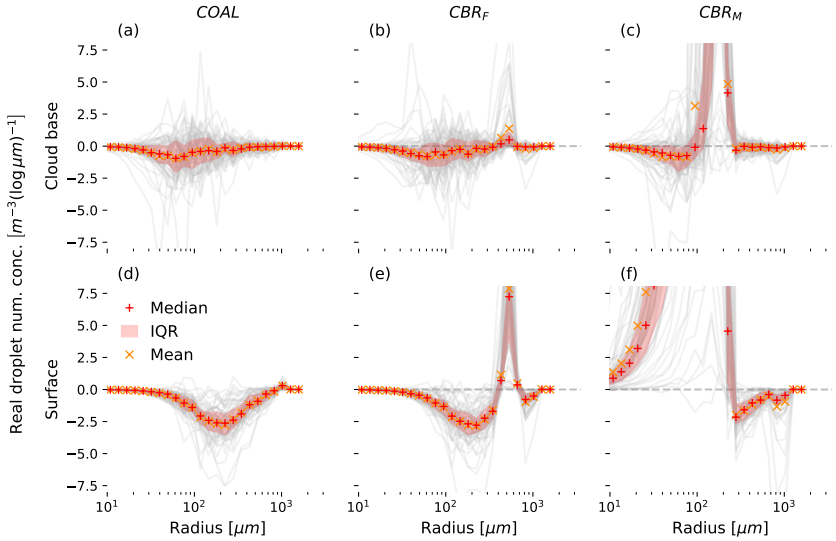

Figure S14: Similar to Figure 14 and Figure 15, but for real droplet number concentration differences

Acknowledgements

I want to thank my supervisors Raphaela Vogel and Joakim Kjellsson as well as Ann-Kristin Naumann for their guidance and input during this study. Also thanks to Mampi Sakar and Shin-ichiro Shima for their constructive input. I want to thank Clara Bayley a lot for her contagious enthusiasm and many hours of fun discussions from all over the globe. Without her intense and constant development of CLEO, this study would not have been possible. Additionally, I want to highlight the community contributions to the development of open-source python packages and analysis tools without whom this work would not have been possible and which are beyond acknowledgements over citations. Big thanks to all the friends and family who made this work possible. Without them, none of this would have been possible at all. And lastly, thanks to wind, waves, and sun for giving me the chance to take plenty of very constructive breaks!

Declaration

I confirm that this master thesis is the result of my own work. No other person's work has been used without acknowledgement in the main text of this thesis. This thesis has not been submitted for the award of any other degree or thesis in any other institution. All sentences or passages quoted in this thesis from other people's work have been specifically acknowledged by clear cross-referencing to author, work and pages. Any illustrations which are not the work of the author of this thesis are specifically acknowledged. The submitted written version of the thesis corresponds to the version on the electronic storage device

Date: _____ Signature: _____